Multi-scale Simulations of Tropospheric Chemistry in the Eastern Pacific and US West Coast during Spring 2002

Youhua Tang[1], Gregory R. Carmichael[1], Larry W. Horowitz[2], Itsushi Uno[3], Jung-Hun Woo[1], David G. Streets[4], Donald Dabdub[5], Gakuji Kurata[6], Adrian Sandu[7], James Allan[8], Elliot Atlas[9], Franck Flocke[9], Lewis Gregory Huey[10], Roger O. Jakoubek[11], Dylan B. Millet[12], Patricia K. Quinn[13], James M. Roberts[11], Eric J. Williams[11], John B. Nowak[11], Douglas R. Worsnop[14], Allen Goldstein[12], Stephen Donnelly[9], Sue Schauffler[9], Verity Stroud[9], Kristen Johnson[9], Melody A. Avery[15], Hanwant B. Singh[16] and Eric C. Apel[9]

1 Center for Global and Regional Environmental Research, University of Iowa, Iowa, USA
2 NOAA Geophysical Fluid Dynamics Laboratory, Princeton, New Jersey, USA
3 Research Institute for Applied Mechanics, Kyushu University, Fukuoka, Japan
4 Decision and Information Sciences Division, Argonne National Laboratory, Illinois, USA
5 Department of Mechanical and Aerospace Engineering, University of California at Irvine, California, USA
6 Department of Ecological Engineering, Toyohashi University of Technology, Toyohashi, Japan
7 Department of Computer Science, Virginia Polytechnic Institute and State University, Virginia, USA
8 Department of Physics, University of Manchester Institute of Science and Technology, Manchester, UK
9 National Center for Atmospheric Research, Boulder, Colorado, USA
10 School of Earth and Atmospheric Sciences, Georgia Institute of Technology, Georgia, USA
11 NOAA Aeronomy Laboratory, Boulder, Colorado, USA
12 Department of Environmental Science, Policy, and Management, University of California at Berkeley, California, USA
13 NOAA Pacific Marine Environmental Laboratory, Washington, USA
14 Aerodyne Research Inc., Massachusetts, USA
15 NASA Langley Center, Virginia, USA
16 NASA Ames Center, California, USA

Abstract:

Regional modeling analysis for the Intercontinental Transport and Chemical Transformation experiment in 2002 (ITCT-2K2) over the Eastern Pacific and US west coast is performed using a multi-scale modeling system, including the regional tracer model CFORS, the STEM-2K3 regional chemical transport model, and an off-line coupling with the MOZART global chemical transport model. CO regional tracers calculated on-line in the CFORS model are used to identify aircraft measurement periods with Asian influences. Asian influenced air masses measured by the NOAA WP-3 aircraft in this experiment are found to have lower ΔAcetone/ΔCO, ΔMethanol/ΔCO, and ΔPropane/ΔEthyne ratios than air masses influenced by US emissions, reflecting differences in regional emission signals. The Asian air

masses in the eastern Pacific are found to usually be well-aged (> 5 days), highly diffused, and with low NO_y levels. Chemical budget analysis is performed for two flights, and the O_3 net chemical budgets are found to be negative (net destructive) in the places dominated by Asian influences or clear sites, and positive in polluted American air masses. During the trans-Pacific transport, part of gaseous HNO_3 was converted to nitrate particle, which attributed to NO_y decline. Without the aerosol consideration, the model tends to overestimate HNO_3 background concentration along the coast region. At the measurement site of Trinidad Head, Northern California, high concentration pollutants are usually associated with calm wind scenarios, implying that the accumulation of local pollutants lead to the high concentration. Seasonal variations are also discussed from April to May for this site. A high-resolution nesting simulation with 12km horizontal resolution is used to study the WP-3 flight over Los Angeles and surrounding areas. This nested simulation significantly improved the predictions for emitted and secondary-generated species. The difference of photochemical behavior between the coarse (60 km) and nesting simulations is discussed and compared with the observation.

1. Introduction:

During April and May, 2002 the Intercontinental Transport and Chemical Transformation experiment in 2002 (ITCT-2K2) studied the airmass characteristics over the eastern Pacific and the US west coast. NOAA WP-3 aircraft and surface measurements were performed with the objective of characterizing the Asian inflow signal and its impact on regional air quality. During this period air masses impacted by Asian emissions are transported to the eastern Pacific by the mid-latitude prevailing westerlies. The long-distance transport of Asian pollutants to the west coast of North America has been studied by many researchers, such as Jaffe et al. (1999) and Kotchenruther et al. (2001). Jacob et al. (1999) discussed the impact of Asian emissions variation on North America air quality using a global model. The strength of the Asian influence on North America was shown to depend on the Asian emission strength and the

transport efficiency over the Pacific Ocean. Asian emissions are comprised of anthropogenic (including biofuel) sources, biomass burning, and volcanic activity. Woo et al. (2003) estimated the biomass burning emission during the spring 2001. Carmichael et al. (2003a,b) studied the features of Asian outflow over the West Pacific and used aircraft measurements and model results to evaluate the emission estimations by Streets et al. 2003. Yienger et al. (2000) described the Asian pollutant transport to North America using CO as the criteria. The trans-Pacific transport of aerosol is also an important issue. During springtime Asian dust storms become active, and dust can be transport to the eastern Pacific and North America (Uno et al., 2001; VanCuren and Cahill, 2002). However, during the ITCT-2K2 experiment the influence of Asian dust on North American was not significant.

To study the transport and chemistry of trace gases and aerosols across the northern Pacific we used a regional chemical transport model. Regional models have an advantage over global models in their ability to use finer resolutions in the analysis, but have the disadvantage of requiring lateral boundary conditions. In this study the lateral boundary conditions were established using a multi-scale modeling system with nested models. Nesting techniques can help in the analysis from two sides: introducing external influences for relatively long-lived transported species, such as CO or O_3 (Langmann et al., 2003), and by considering high-resolution emissions for short-lived species, such as NO_x or SO_2 (Tang, 2002). High-resolution emissions can more accurately resolve near-source concentrations, and better estimate photochemical budgets (Tang, 2002).

In this paper the multi-scale model is used to help analyze aircraft and surface measurements obtained during the ITCT-2K2 experiment. In the following section the details of the model are presented. In Section 3 Asian tracer information calculated by the model is used to classify the aircraft observations into those observations with large and small Asian signals, which are then subsequently used to help quantify observed characteristics of Asian air masses over the Eastern Pacific. Specific characteristics of

individual aircraft flights are analyzed in Section 4, where the multi-scale model system is used to study the photochemistry in air masses over the eastern Pacific as aged air masses interact with emissions from North America. The WP-3 flight on May 13 over Los Angeles is analyzed as an example of the effect of model resolution on model predictions. The effect of aerosols on nitrate partitioning is presented in Section 5. Results from a fine-scale nesting simulation of the flight around Los Angeles are presented in Section 6. A mission-wide perspective of the performance of the model comprises Section 7. Analysis of the Trinidad Head observations is presented in Section 8.

2. Model System:

Characterizing the Asian influence on the chemistry of the eastern Pacific is a challenge as trace species are diluted during their trans-Pacific transport, which makes it difficult to distinguish them from background conditions. These air masses also mix with local sources as they move in-land. To efficiently consider these processes a multi-scale model system was established. This model system includes the MOZART global chemical transport model (Horowitz et al., 2003), the inter-continental chemical tracer model CFORS (Uno et al., 2003), and a nested regional chemical transport model, STEM-2K3 (Tang et al., ACE-Asia issue). The model domains are shown in Figure 1.

CFORS is an on-line tracer model (Uno et al., 2003) coupled with the RAMS regional meteorological model. In this application CFORS was driven by NCEP reanalysis for post analysis and AVN data for forecasting uses. CFORS treats chemical species as tracers assuming linear consumption. For example, NO_x tracer in CFORS decays with a first-order rate:

$$\frac{d[NO_x]}{dt} = -k_{NOx}[NO_x] \qquad (1)$$

where k_{NOx} is a fixed value. In CFORS, we define a conservative NO_y (total odd nitrogen species) tracer that can be transported without loss, and assume that this NO_y tracer has the same emission source as NO_x. Under this assumption, the NO_x age can be derived from equation (1):

$$T_{NOx} = k_{nox} \ln([NO_y]/[NO_x]) \qquad (2)$$

This equation allows for the on-line calculation of the averaged NO_x age when air masses from different sources mix together. This NO_x age represents a combined result of transport time, diffusion, and NO_x source intensities. With the same method we also define a VOC (volatile organic compounds) age using ethane as an indicator that is related to ethane emission and decay rate. In this study, the decay rates used in CFORS for CO, SO_2, NO_x and ethane were 2.22×10^{-7}, 2.78×10^{-6}, 9.26×10^{-6} and 1.25×10^{-7} s^{-1}, respectively.

CO is one of the primary tracers in CFORS and is used to help classify emission source types and regions. In this study CO was parsed into: Asian anthropogenic, biomass burning (BB), Mexico, Canada, California, Washington-Oregon, and the rest of the USA. These regional CO tracers can be used to help determine the airmass properties and its mixing state. During the ITCT-2K2 field campaign forecast products for these tracers were also used for flight planning. It is important to note that these CO tracers in CFORS do not yield a total CO value that can be quantitatively compared to observed values because they represent primary CO only. The CFORS analysis does not consider CO that arises from methane and non-methane hydrocarbon oxidation. Furthermore the background levels were set to zero. In this paper, CFORS tracer model for ITCT-2K2 used a domain with 100×42 grids with a 200 km horizontal resolution (Figure 1), which covers East Asia, the northern Pacific Ocean, and most North America.

Comprehensive chemistry and transport interactions are calculated by the STEM-2K3 regional chemical transport model, which is a further development of the STEM-2K1 model (Tang et al., 2003a; Carmichael et al., 2003a) that includes the SAPRC-99 gaseous mechanism (Cater, 2000) and an explicit photolysis-

rate solver (the on-line TUV (NCAR Tropospheric Ultraviolet-Visible radiation model, Madronich and Flocke, 1999)). The main improvement of STEM-2K3 over STEM-2K1 is that the former also includes an aerosol thermodynamics module, SCAPE II (Simulating Composition of Atmospheric Particles at Equilibrium) (Kim et al, 1993a, b; Kim and Seinfeld, 1995), for calculating gas-particle equilibrium concentrations among inorganic aerosol ions and their gaseous precursors. Tang et al. (ACE-Asia issue) described the framework of STEM-2K3 and its performance during the TRACE-P (TRAnsport and Chemical Evolution over the Pacific) (Jacob et al., 2003) and ACE-Asia (Aerosol Characterization Experiment in Asian Pacific Region) experiments. In this paper the analysis includes inorganic aerosols in 4 size bins (in diameter): 0.1μm-0.3μm, 0.3μm-1.0μm, 1.0μm-2.5μm, and 2.5μm-10μm, (referred to as bins 1 to 4, respectively). Daily TOMS (Total Ozone Mapping Spectrometer) data was used to calculate the model's overtop ozone column needed in the photolysis calculations using the TUV module.

The primary domain for STEM-2K3 covers the U.S. west coast and eastern Pacific with a 60km horizontal resolution (Figure 1). Another RAMS model run in this domain was used to drive STEM-2K3. To better reflect the influence of more local sources, such as during the flight over the Los Angeles basin, a higher resolution is necessary. Here a nested domain with a nesting ratio of 1:5 (Figure 1) was used. The nested STEM-2K3 was driven by meteorology interpolated from the RAMS 60km predication. The change in resolution affects the emission intensity. For example, Figure 1 shows that CO emission rate in Los Angeles ranges from 150 to 300 mole/hour/km^2 represented in the domain of 200 km resolution, is over 1500 mole/hour/km^2 in the 60 km domain, and greater than 3000 mole/hour/km^2 (peak value) with 12 km resolution. Tang (2002) discussed how model resolution affected O_3 and NO_x predications, and photochemical correlations through for the TRACE-P and ACE-Asia experiments.

2.1 Lateral Boundary Conditions

The MOZART global model was used to provide lateral boundary conditions for the STEM-2K3 primary 60km domain (Figure 1) applications. The lateral boundary and top boundary conditions of STEM-2K3 for all species except CO were interpolated to the primary 60 km domain from the MOZART model results produced using NCEP winds. Due to the uncertainties in the CO emission inventories the global model tends to quantitatively underestimate CO in the mid latitudes and altitudes. The ITCT-2K2 aircraft observations showed that CO had a stable background concentration over the Eastern Pacific, and CO contributions from various sources were mostly represented by enhancements above background. In this paper, we set the boundary condition of STEM-2K3 for CO to the background CO (shown in Table 1) plus a perturbation calculated as the total tracer CO from the CFORS model. The boundary values above the flight altitude of the WP-3 were obtained using the observations by the NASA DC-8 aircraft during the TRACE-P experiment. Table 1 also shows the model vertical layers used in CFORS and STEM-2K3, defined in the mid-point of the RAMS sigma-z layers (Pielke et al., 1992). The nested 12km domain has the same vertical layers as the 60 km primary domain, and the lateral boundary conditions were also interpolated from the 60 km domain.

2.2 Emissions

Emission data used in this study came from various sources. The basic strategy to develop the assembled emissions inventory was to use global scale emissions inventories as background/lower quality assurance information, and to supplement these with more comprehensive/higher quality regional scale emissions data for Asia and North America regions. The Asian anthropogenic emissions were based on the estimate of Streets et al. (2003a; 2003b). Biomass burning emissions for Southeast Asia were based on April-averaged Asian BB emissions for the base year of 2001 (Woo et al., 2003). Emissions in the United State and Canada were based on the USEPA 1996 inventory. Mexican emissions came from Kuhns (2001). The ship emissions for CO, SO_2 and NO_x were based on the inventory of Corbett et al. (1999), and aviation emissions were taken from EDGAR (Olivier et al., 1996). Lightning NO_x emissions were diagnosed from

the meteorological model according to deep convective intensities (Pickering et al., 1998). Emissions for all other regions in the 200 km domain came from GEIA inventory (Global Emissions Inventory Activities, http://geiacenter.org/). Biogenic emissions for the regions other than the United States come from GEIA (Guenther et al., 1995). MOZART global model has it own emission (Horowitz et al., 2003), which is mainly based on the EDGAR inventory (Olivier et al., 1996).

For simulating pollutant re-circulation from the western U.S. into the Pacific Ocean and propagation from the West Coast inland, we used US EPA emission databases and more detailed allocation procedures. For example, the emission data for the nested 12km domain (Figure 1) requires a resolution higher than county scale. The original county-scale emissions were redistributed to the finer resolution grid system using high-resolution population data to give "within county" spatial variability. Further detail into the methodology for this approach used to generate high-resolution emissions for nested simulations can be found in the references elsewhere (Woo et al., 2003; Tang, 2002).

3. Air-mass Characteristics

The NOAA WP-3 aircraft performed 13 flights, including transit flights to and from the base in Monterey, California (Figure 1). One objective of these flights was to characterize Asian air masses over the eastern Pacific and how they are modified as they move over the American continent and mix with local sources. Identification of air masses impacted by Asian emissions is difficult due to the long transport times and the variety of sources impacting the Pacific Basin. Techniques for identifying Asian emission signals that rely on observation-based filters are discussed in Nowak et al. and de Gouw et al. (this issue). Alternatively the model can be used to identify those air masses expected to contain Asian signals. We used an Asian air-mass ratio, defined as the Asian anthropogenic CO tracer concentration divided by total anthropogenic tracer CO concentration in this domain, to identify air masses impacted by Asian sources. This metric was calculated for each WP-3 3-minute flight segment, and the aircraft data was then sorted

using the model calculated Asian ratios. Figure 2 shows correlations of observed species for air masses with Asian ratios < 20% and those with values > 80% using the 3-minute merged data set for all ITCT WP-3 flights. The data points with Asian ratio < 20% and > 80% account for about 23% and 53% respectively in all WP-3 flights. Figure 2 also shows the airmass correlations of the observations taken on-board the NASA DC-8 and P-3B aircrafts over the Western Pacific during the TRACE-P experiment, March of 2001. Figures 2a and 2b show that Asian air masses have lower $\Delta NO_y/\Delta CO$ values in both the Western Pacific and Eastern Pacific than air masses dominated by American emissions. Tang et al. (2003b) found that BB plumes from Southeast Asia have low $\Delta NO_y/\Delta CO$ ratios (about 0.005 ppbv/ppbv). Asian air masses impacted by biofuel sources exhibit similar low ratios. The portion of emissions from gasoline in Asia is generally smaller than that in the United States (Streets et al., 2003). For example, coal is the main fossil fuel used in China, and coal combustion also emits a lower $\Delta NO_y/\Delta CO$ than gasoline combustion. All these factors contribute to Asian air masses having a ~10 times lower $\Delta NO_y/\Delta CO$ ratio than American air masses. After long-distance transport the ratio in the Asian air masses decreases to ~0.0035 ppbv/ppbv (Figure 2a) due to NO_y's gas-particle conversion, and wet and dry depositions. This is discussed further in Section 5.

The air masses dominated by American sources show higher correlation coefficients than Asian air masses for CO versus acetone and methanol (Figures 2c-2f). These results imply that CO, acetone and methanol in the United States come from similar emission sources. Air masses with Asian ratios < 20% have higher ΔAcetone/ΔCO and ΔMethanol/ΔCO ratios, reflecting the large petroleum refining and usage in the western USA.

The lifetimes of propane and ethyne range from several days to several weeks. However, they have similar reaction rate with OH, the main reaction for their consumption. Figures 2g and 2h show that the ΔPropane/ΔEthyne ratio associated with Asian sources (1.2 ppbv/ppbv) is 70% lower than in American

air masses, but still higher than the TRACE-P measurement since Asian air masses in the eastern Pacific are mixed with North American sources.

The values presented above based on a model-based screening for Asian plumes can be compared to values calculated based on observation-based plume identification. An observation-based Asian plumes value of $\Delta NO_y/\Delta CO$ for the May 5 flight for altitudes > 5km of 0.003 ppbv/ppbv was reported by de Gouw et al. (this issue), while values of 0.0035-0.0049 ppbv/ppbv for all identified Asian plumes were calculated by Nowak et al. (this issue). In terms of ΔPropane/Δethyne, observed values ranged from 1.5 to 1.1 ppbv/ppbv for the May 5 and May 17 flights, respectively, which represent the two most heavily influenced Asian events. These results indicate that the model-based approach provides a consistent and 4-dimensional contextual method to help identify Asian air masses.

The observations also provide indicators of ozone production. NO_z (NO_y-NO_x) represents the oxidized products of NO_x, including peroxyacetyl nitrate (PAN), HNO_3, HNO_2 et al. The ratio $\Delta O_3/\Delta NO_z$ represents the upper limit of the ozone production efficiency (OPE) per unit NO_x (Trainer et al., 1993). Figure 2i shows this ratio for the air masses with Asian ratios < 20% and > 80%, and O_3 and NO_z have relatively strong correlations in both sets of data. The $\Delta O_3/\Delta NO_z$ ratio in Asian air masses over the Eastern Pacific is higher than that in American air masses and in air masses over the Western Pacific (Figure 2j). The very high $\Delta O_3/\Delta NO_z$ of Asian air masses over the Eastern Pacific (Figure 2i) is not solely due to the accumulation of NO_x photochemically generating O_3. The NO_z conversion to nitrate aerosol and depositions also results in an increase in this ratio**.** This was shown to be important in the Asian outflow during ACE-Asia, and where most of the nitrate was concentrated in the super-micron particles, and thus were more rapidly removed from the air via deposition processes (Tang et al., 2003).

Classification of the air mass age is an important element of analysis. Air mass age can be estimated from trajectory analysis (Cooper et al., this issue). This can also be done using observed chemical ratios as discussed by de Gouw et al. (this issue). The multi-scale model also includes indicators of chemical age. Figure 3 shows the observed Propane/Ethane and NO_x/NO_y ratios plotted against predicted CFORS VOC and NO_x ages, respectively. The aircraft measurements indicate that fresh air masses from the United States have Propane/Ethane ratios > 1, but air masses with ages > 50 hours have ratios < 0.4. The main consumption of propane and ethane in the atmosphere is through reactions with OH, and the reaction constant for propane is about four times bigger than that for ethane. Figure 3a shows that the Propane/Ethane ratio declines very fast within the first 50 hours. After 50 hours this ratio takes values between 0.02-0.3. The relation between observed NO_x/NO_y and predicted NO_x age (Figure 3b) is similar to that between Propane/Ethane and VOC age. The best-fit lines in Figure 3 show the lower limits to be 0.1 for Propane/Ethane, and 0.08 for NO_x/NO_y.

The points in Figures 3a and b are color-coded using CFORS VOC age. The results for the NO_x age show that the two age metrics produce consistent results. The fraction of NO_x in NO_y shows more variability at a given age than the Propane/Ethane ratio, which reflects the complexity of the NO_x chemistry relative to that for propane and ethane. In fresh polluted air masses NO_x usually is converted to NO_z through photochemical reactions, and O_3 is one of the by-products during this conversion. However, some reactions, such as the photolysis of PAN, recycle NO_z back to NO_x. The ITCT measurements indicate that some NO_y enhancements at high altitudes were associated with stratospheric intrusions, implying that stratospheric contribution to NO_y or NO_x via N_2O dissociation (Strahan, 1999) could be significant for these flights.

4. Case Studies

The multi-scale modeling system was used in forecast-mode for flight planning, and in post analysis mode to help interpret the observations. The air mass age discussion in the previous section indicated that the air masses from Asia took on the order of one week to reach the Eastern Pacific. During this transport journey dynamic mixing and dispersion processes act to decrease the air mass concentrations. This fact, coupled with the complexity of the interactions between aged air masses and fresh emissions from the western US, make it difficult to interpret the observations. Here we show how the various model products can aid in the analysis and how the observations help to evaluate the model performance. These aspects are explored through the analysis of individual flights. The flights discussed above focus on typical flights that involve a mixture of local and Asian influences.

4.1 WP-3 Flight on April 25

On April 25, the NOAA WP-3 aircraft performed its second flight along the California coast (Figure 4), and encountered aged Asian air masses mixed with American pollutants. In the model's 1 km layer over most of the domain, with the exception of the continental US, the anthropogenic CO Asian ratio is higher than 0.8 (80%) (Figure 4a). Figure 4b shows that Asian sources have a stronger impact on CO over North America at higher altitudes. Figures 4c and 4d show simulated O_3 over the eastern Pacific and the WP-3 flight path, which was located near a low-pressure system. At low altitudes (Figure 4c) O_3 was formed over the western US and transported out over the ocean, as shown by the band with $O_3 > 55$ ppbv that extends southwestward from northern California. The oceanic area with $O_3 > 45$ ppbv west of Mexico is associated with an aged polluted airmass comprised of a mixture of Asian and North American air (as shown by the Asian ratio <0.6 as shown in Figure 4a). In the higher altitudes ozone concentrations were mainly maintained by downward transport of stratospheric ozone (Figures 4d and e).

Figure 4e shows the cross–section of O_3 concentration and chemical net budget along latitude 35°N, a section that approximates the path of the WP-3 flight 2. Simulated O_3 showed a net loss over the ocean

areas and above 3 km over land, and a net production below ~3 km over the polluted regions near Los Angles. In the low altitudes over the ocean, O_3 had the highest loss rates and lowest concentrations because the high water vapor conditions within the marine boundary layer (MBL) benefited the $O^1D + H_2O \rightarrow 2OH$ reaction, which reduced the chance of O^1D converting back to O_3 via $O^1D + Air \rightarrow O^3P$ and $O^3P + O2 \rightarrow O_3$. Due to the high OH production in the MBL the CO net chemical budget was ~ -0.3 ppbv/hr (Figure 4f). The CO chemical budget became positive only over the polluted regions where hydrocarbon oxidization was important.

Figure 5 compares measurements of WP-3 flight 2 with simulated values extracted along the flight path. The tracer-CO results are plotted in Figure 5a. The CO Asian ratios varied by height, with values > 65% and <40% for the flight altitudes higher than 3 km and lower than 2km, respectively. Asian air masses are usually transported across the Pacific in the mid to upper troposphere, and brought to lower altitudes through convective exchange and subsidence. At low altitudes over inland locations, such as the flight path around 18:55 GMT, the CO Asian ratio fell below 10%. For short-lived species, like NO_x and SO_2, the Asian influence is small due to removal and conversion processes during the long-distance transport. Figure 5b shows that the STEM simulation was able to capture the main observed ozone features. The calculated ozone net photochemical budget is also presented and the net budget reached a maximum positive value around 18:55GMT, when the aircraft flew inland at low altitudes. At other flight locations the O_3 chemical budget was negative.

Figure 5c shows that modeled CO exhibits much less variability than that observed, and underestimated the observed CO by more than 10 ppb during 19:00-21:00 GMT. The calculated CO chemical budget was positive when the pollutant loading was high, reflecting CO produced from non-methane hydrocarbon (NMHC) oxidation. For other locations the CO budget was always negative and CO consumption via reaction with OH dominated. The chemical net budget for PAN is similar to that of CO. PAN was

chemical formed over polluted areas, while photolytic loss was the main reason for the negative budgets at clean locations. Figure 5 also shows that the STEM model accurately predicted J-values (photolysis rates) for J[$O_3 \rightarrow O_2 + O^1D$] and J[$NO_2 \rightarrow NO + O^3P$] using the on-line TUV. The agreement between the simulation and measurement for J[O^1D] is better than that for J[NO_2], since J[NO_2] is sensitive to long-wavelength radiation, which can be affected by fractional clouds (a quantity that is difficult to model). This flight encountered some fractional clouds. Figure 5f shows that several of the peak values for J[NO_2] above 4km were not predicted by the model and these could be associated with fractional clouds. Similar results were found for J-values over Western Pacific during TRACE-P as discussed by Tang et al. (2003a).

To explore the photochemical system during this flight three points along the flight path were further analyzed. The WP-3 aircraft observations at 19:00, 19:03 and 21:00 GMT were selected. The points at 19:00 and 19:03 GMT were when the aircraft made a vertical ascent downwind of Los Angles. The model simulation shows disparate air massses at the beginning and end of this profile, with the predicted CO Asian ratio of 10% at 19:00GMT and 64% at 19:03GMT. When air masses from the Pacific Ocean moved on-shore during the daytime an internal boundary layer (IBL) formed (Garratt, 1990) which in the model extended to ~2 km. Within the boundary layer the air was mixed with local pollutants transported from Los Angeles and surrounding area. Above this boundary layer, the air preserved its aged Asian features. The point at 21:00GMT was at the west end of this flight at low altitude over the Eastern Pacific.

Figure 6 shows the simulated chemical production and loss terms for O_3, CO, OH, HO_2 and HCHO at these three points. The O_3 budget components (Figure 6a) show that O_3 had a positive budget and the highest photochemical generation through $O^3P + O_2 \rightarrow O_3$ (R#2 in Table 2) at 19:00GMT in the polluted airmass. O_3 also had a lower photolysis rate (R#17 and R#18 in Table 2) at 19:00GMT than at 19:03GMT due to the altitude dependency of the actinic flux. At 19:03GMT the O_3 net budget was near zero. When

the WP-3 aircraft flew at low altitude over the clean oceanic area at 21:00GMT the O_3 budget was negative because of the rapid consumption of O^1D in the water rich MBL via $O^1D + H_2O \rightarrow 2OH$ (R#19 in Table 2), as was also discussed for Figure 4e.

Under these conditions there is higher OH production (Figure 6c) and CO net loss (Figure 6b) at 21:00GMT. Figure 4b shows that the polluted airmass encountered at 19:00GMT had the highest CO consumption through R#29: $CO + HO + O_2 \rightarrow HO_2 + CO_2$ due to its high OH and CO concentrations. However, this polluted point also had the highest CO production among these three points due to oxidation and photolysis of aldehydes. The simulation indicates that most of the aldehydes were intermediate products of hydrocarbon oxidization at 19:00GMT, and that the hydrocarbon oxidation offset part of CO loss, resulting in a net positive CO budget in the polluted area (Figure 4f). The two clean locations at 19:03GMT and 21:00GMT had similar low concentrations for most hydrocarbons and aldehydes, but the OH production in the MBL at 21:00GMT was high, resulting in the highest CO net loss among these three points.

Figure 6c shows that the polluted point of 19:00GMT had the highest OH concentration, mainly due to the additional OH production through R#31: $NO + HO_2 \rightarrow OH + NO_2$. In polluted areas the following reactions are important:

$$CO + OH + O_2 \rightarrow HO_2 + CO_2 \qquad R\#29$$

$$HO_2 + NO \rightarrow NO_2 + OH \qquad R\#31$$

$$NO_2 + hv \rightarrow NO + O^3P \qquad R\#1$$

$$O^3P + O_2 \rightarrow O_3 \qquad R\#2$$

$$O_3 + hv \rightarrow O_2 + O^1D \qquad R\#18$$

$$O^1D + H_2O \rightarrow 2OH \qquad R\#19$$

This series of reactions is constrained by NO_x and NMHC concentrations. Under optimal NO_x and NMHC conditions these reactions effectively produce OH. The point at 19:00GMT reflects this situation, and high OH concentrations were observed downwind of Los Angeles, which will be discussed later. Under low NO_x conditions these reactions can not be performed completely, and Figure 6c shows that the reaction rates of R#31 at 19:03GMT and 21:00GMT were much lower than that at 19:00GMT. The reaction rate of R#19 was highest at 21:00GMT due to its rich water vapor, which resulted in elevated OH concentrations, though still lower than that at the polluted point. At the polluted point OH increased by converting HO_2 to OH. Here HO_2 concentrations were maintained (Figure 6d) by HO_2 production via reactions R#46, R#51, R#123 and R#125 that converted RO_2 and HCHO to HO_2. RO_2 and HCHO were produced as intermediate products of hydrocarbon oxidization. Figure 6d shows that the MBL site had the highest HO_2 concentration, due to high OH (for R#29) and low NO_x (for R#31) concentrations. Figures 6c and 6d illustrate the impact of fast conversion between OH and HO_2, and their connection to external sources. R#19 was the main external source for HO_x at the MBL, and RO_2 and aldehydes were the main precursors of HO_x at the polluted site.

Figure 6e shows that HCHO had negative budgets at all these sites, and the MBL site had the highest HCHO net loss due to its high OH. The polluted point at 19:00GMT had the highest HCHO consumption, but it also had the highest HCHO production from hydrocarbon oxidization. At the clean points HCHO mainly came from methane oxidization $CH_4 + OH + O_2 \rightarrow CH_3O_2 + H_2O$ and $CH_3O_2 + NO + O_2 \rightarrow NO_2 + HCHO + HO_2$ (R#46 in Table 2), which was constrained by NO_x availability. Other production pathways, such as $CH_3O_2 + CH_3O_2 \rightarrow CH_3OH + HCHO + O_2$, were usually small. The production of HCHO was not sufficient to offset HCHO consumption except in heavy polluted areas. At the 19:00GMT point the pollutants were already diluted, and the HCHO net chemical budget was negative.

4.2 WP-3 Flight on May 15

The 11th NOAA WP-3 flight flew west to 129°W over the Eastern Pacific on May 15 (Figure 7). This flight encountered aged Asian and American air masses. Figure 7a shows that CO Asian ratio was high over most of the Eastern Pacific in the model's 1 km layer. Some fresh air masses with Asian CO > 15 ppbv approached this region, but did not arrive at the WP-3 flight path. Along the North American coastline CO Asian ratios showed a strong gradient. At 5.4 km (Figure 7b) the CO Asian ratio was higher than 0.9 throughout the domain north of 30°N, which reflects the high transport efficiency in mid to high latitudes and high altitudes. The influence of American sources was concentrated to inland areas at low altitudes. The WP-3 flight region was ahead of a cold front, and north winds dominated (Figures 7c, 7d, and 7e). The pre-frontal ascending winds transported low O_3 concentrations from the MBL to higher altitudes, and the post-frontal descending air caused a high O_3 zone around 155°W, 44°N, which was shown in all the layers (Figures 7c, 7d and 7e). It should be noted that the relatively fresh Asian air masses (northwest corner of this domain) were also transported mainly from the high altitudes due to the high transport efficiency.

Figures 7f, 7g and 7h show the O_3 chemical net budget in the 1 km, 2.8 km and 5.4 km layers. In the l km layer O_3 net production was high over polluted inland areas and in the fresh Asian air masses (Figure 7f). The distribution of O_3 concentrations (Figure 7c) shows high concentrations in regions with positive net budgets, indicating that the O_3 chemical budget was the dominant factor affecting O_3 concentrations in the low altitudes. In the 2.8 km layer transport effects were important as shown by the fact that the O_3 chemical net budget was negative (< -0.1 ppbv/hr) over most of California, but O_3 concentrations were still higher than background (> 65 ppbv) over most Southern California. In the 5.4km layer transport effects dominated. Figure 7h shows that the O_3 net budget was negative over most of this domain, but very high O_3 concentrations (> 100 ppbv) existed in some areas due to the stratospheric influence. Under

these conditions elevated O_3 levels can correspond to areas with strong O_3 loss caused by photolysis, such as the high-O_3 zone around 112°W, 48°N.

The CO net budget distribution is similar to O_3 in the 5.4km layer, as O_3 loss is mainly through its photolysis process, and the O^1D produced forms OH (via R#19 in Table 2) which consumes CO. Under these conditions O_3 loss is usually correlated with CO loss. Figures 7i, 7j, and 7k show that the CO net budget is positive only over heavily polluted areas and their downwind sites rich in hydrocarbons. At high altitudes the CO budget was always negative.

The WP-3 flight 11 flew a triangle flight path over the Eastern Pacific (Figure 7f), with its west end longitude reaching about 129°W. In contrast to the WP-3 flight 2, this flight had some low-altitude points with possible strong Asian signals (cf, 20:50GMT, Figure 8a). At higher altitudes (> 3km) the CO Asian ratio was greater than 0.8. Figure 8a shows that the CO Asian ratio was lower than 30% only in the low-altitude near-coast flight segments. The STEM simulated CO agrees well with the observations (Figure 8b), and the simulated CO budget shows that net CO production occurred only in the departing and arriving segments, near the polluted San Francisco bay area.

Figure 8c shows the O_3 concentration comparison and simulated O_3 net chemical budget. The calculated ozone captured many of the large-scale features (including the altitude dependency), but was not able to resolve the finer scale features observed. The simulated O_3 net chemical budget for this flight is similar to that of flight 2. The model accurately captured ethyne values as shown in Figure 8d. Since ethyne has no photochemical sources its net chemical budget is always negative, and mainly determined by local OH concentrations, even over polluted area. The variation of ethyne chemical budget is very similar to that of CO over ocean since both are determined by the OH concentration. The OH concentration was very sensitive to photolysis rate, and the model reasonably simulated the observed J-value behavior (Figure 8e,

8f). Most of the areas that the WP-3 flight 11 flew over were under clear-sky conditions, and the photolysis rates were mainly affected by altitude and sunlight zenith angle. Figure 8g shows the comparison for PAN concentrations and the simulated PAN chemical budget, which are similar to those for O_3 (Figure 8c). The PAN formation is mainly through photochemical reaction between NO_x and NMHCs, and its loss is mainly caused by its photolytic destruction.

The WP-3 flights 2 and 11 represent the situation typically encountered by most flights over the Eastern Pacific and the near-coast regions. In these flights Asian air masses impacted by Asian sources dominated at altitudes above 4 km, but had little effect over the inland low-altitude areas. Since aged air masses usually were low in NO_x the O_3 photochemical production was low and the net chemical budgets were negative in the Asian air masses arriving over North America.

5. Nitrate Partition

Tang et al. (ACE-Asia issue) discussed nitrate partitioning between the gas and aerosol phases for the ACE-Asia and TRACE-P experiments, and found that the regional model without aerosol considerations tended to overestimate nitrate acid (HNO_3). Similar results (Neuman et al., 2003) were found for the ITCT-2K2 flights along the coast where regional pollutants interacted with sea salt, resulting in some of the nitric acid partitioning into the sea salt particles. Figure 9 shows the simulated HNO_3 mixing ratios with and without aerosol uptake compared to the measurements for WP-3 flights 4, 5, 8 and 9. The simulation with aerosol uptake had lower HNO_3 concentrations than the simulation without aerosol for most segments of these flights. Due to the relatively coarse horizontal resolution, the simulation with aerosol underestimated most of the HNO_3 peak values. The most significant differences between these two simulations appear for the predictions for background HNO_3 levels. The simulation without aerosol uptake systematically overestimated the low background concentrations, especially for WP-3 flight 5, and it overestimated the HNO_3 peak value for WP-3 flight 4. Under cation-limited conditions the simulation

with aerosol uptake can yield higher HNO_3 values (Figure 9b) due to competition effects involving sulfates. However, over most clear oceanic sites, aerosol uptake tended to reduce gas phase HNO_3. This partitioning is an important factor causing the very low NO_y ratio in the long-distance transported Asian air masses (Figures 2a and 2b).

6. Nested Simulation for the Los Angeles plume

The WP-3 flight 10 performed an urban plume study over Los Angeles (LA) and surrounding areas. For this flight the contribution of Asian sources were small. The primary domain over the Eastern Pacific (Figure 1) with its 60 km horizontal resolution was not able to capture the fine structures caused by local emissions. Tang (2002) tested the multi-scale simulation using nested domains in Nashville, Tennessee, and found that nesting predictions could better reflect power plant and urban plume structures. When the 10th WP-3 flight flew over LA and its downwind areas it encountered strong local plumes with steep concentration gradients, implying that local emissions played the dominant role on species concentrations. To simulate this scenario, a domain with a 12 km horizontal nested grid within the primary Eastern Pacific domain (Figure 1) was used. Simulated CO and O_3 concentrations in the coarse and fine domains are shown in Figure 10. The coarse and fine simulations produced qualitatively similar CO and O_3 distributions, but the higher resolution highlights the fine-scale structures. During this flight a front passed over LA region. Figure 10a shows that the low-altitude winds came from the northwest, and turned southwesterly after passing over LA. In the upwind areas, west of longitude 119°W, the coarse and nesting simulations did not show significant differences for O_3 and CO. Over and downwind of LA the nesting simulated CO showed two high zones (Figure 10a), while the coarse simulation had only one broad high-CO region (Figure 10b). The CO distributions mainly reflect the local emissions and transport effects. The elevated O_3 regions in the nested-grid simulated did not overlap with the peak values of CO (as was the case for the coarse simulation), but instead were shifted downwind. The region of high ozone

(> 120 ppbv) was significantly smaller on the fine grid, indicating the effect of model resolution on photochemical processes.

To highlight the differences between these two simulations the flight segment shown in Figure 10c, where the WP-3 aircraft operated around in and around LA, was analyzed further. Figure 11 shows these two simulations compared to the aircraft measurements. The simulated ethyne and propane concentrations using the nested grid were in much better agreement with the observations (Figure 11a, 11b). This is mainly due to the better resolution of the emissions, which enables a better representation of peak values. The refined high-resolution emissions better resolve the differences among urban, suburban and rural areas.

The lifetime of CO is much longer than ethyne or propane, and it also has a higher background concentrations and stronger emissions. Thus CO concentrations reflect the impacts of both local emissions and transport. Both the coarse and fine grid simulated CO capture the main altitude variations (Figure 11c), but the nested grid better represents the CO fine structures. Figure 11c also shows the simulated CO chemical net budgets, which vary in a manner consistent with that for the CO concentrations. The CO chemical budget is determined by the oxidations of CO and hydrocarbons. In the low-altitude areas around LA hydrocarbons were elevated and CO had a positive net chemical budget that was positively correlated with the hydrocarbon concentrations. Most primary hydrocarbons tend to be co-emitted with CO in this region, and thus high CO concentrations usually correspond to high hydrocarbon concentrations (Figures 11a, 11b, 11c). This is the reason why the CO net budget was correlated with CO concentration. For this flight the CO positive chemical budget helped to maintain the high CO concentration, but the high CO was mainly caused by strong emissions. The contribution of the CO chemical budget to CO concentrations was relatively weak, less than 2.5 ppbv/hour (Figure 11c).

Both the fine and coarse grid simulations tended to overestimate O_3 concentration, but the nested one shows better agreement with the observations (Figure 11d). The net O_3 chemical budget for most of the flight segments was positive, up to 25 ppbv/hour. For the flight segment after 21:40 GMT the O_3 concentrations followed the variations in the O_3 chemical net budgets, implying that O_3 production was the dominant influencing factor for O_3 concentrations (as expected). The O_3 chemical budgets on the fine grid show larger absolute values and variation than for the coarse grid, consistent with the better ability to resolve plume-like structures using the finer grid. The 12 km simulation improved the O_3 prediction, but even finer grids are needed.

The improvement in ozone prediction with finer grids can be explained by looking at the predicted and observed NO_z (NO_y-NO_x) concentrations (Figure 11e). As the photochemical product of NO_x, NO_z is usually highly correlated with O_3 (Trainer et al., 1993). The fine grid simulation shows a much better agreement with the observations, and the coarse grid tends to overestimate NO_z. Figure 11e also shows the O_3/NO_z ratios. Both simulations agree well with the observations for the flight segment before 22:00 GMT, but tend to underestimate this ratio (especially for the coarse simulation) by overestimating NO_z between 22:00 GMT and 23:00 GMT. The OPE difference between these two simulations and the observations reflect their different photochemical behaviors, which is also highlighted by their OH differences (Figure 11f). Both simulations systematically overestimated OH, but the nested simulation showed improvement for some flight segments (e.g., 22:30GMT to 23:30GMT). However, the OH overestimation is not caused by overprediction of the J-values. Figures 11g and 11h show $J[O_3 \rightarrow O_2 + O^1D]$ and $J[NO_2]$ simulations compared to the observations. $J[O_3 \rightarrow O_2 + O^1D]$ is a key factor for clear-background OH, since $O^1D + H_2O \rightarrow 2OH$ (R#19 in Table 2) is the primary natural source of OH. The simulation agrees well with the observations for $J[O_3 \rightarrow O_2 + O^1D]$, but overestimates $J[NO_2]$. However, the $J[NO_2]$ overestimation is much smaller than the OH or O_3 overestimations for the flight segments before 23:00GMT, indicating that OH overestimation may be associated with other process. The observed peak

of OH appeared downwind of LA at low-altitude (23:00GMT in Figure 11f) where the observed J-values were very low (Figures 11g and 11h). This implies that other photochemical processes had stronger influence on OH than the R#19 only in the polluted area, which was also discussed before (Figure 6). Tang (2002) showed that nested simulation could have different photochemical relationship from the corresponding coarse simulation. In this WP-3 flight segment, these two simulations showed different responses to the same J-values, due to their different pollutant loadings. Figure 11 shows that the nested simulation yielded better agreement with the observation than the coarse one for most flight segments, implying the impacts of changing resolution on emitted species, secondary-generated species and photochemical system.

7. Mission-Wide Summary

The aircraft observations provide a valuable data set upon which to evaluate the models capabilities to simulate trace species distributions in the Eastern Pacific. A mission-wide summary of the model predicted and observed values are shown in Table 3. Presented are mean values for all 3-minute averaged observations and simulated values for the 13 WP-3 flights parsed into and averaged over three altitude layers. Also shown are the correlation coefficients (R). The RAMS model driven by NCEP reanalysis data accurately represented the meteorological variables as shown for pressure, wind speed and relative humidity. In terms of trace gas species the highest mean concentrations are generally found below 1 km, indicative of the fact that low altitude flights tended to sample air dominated by emissions from North America. PAN, HNO_3, and acetone showed highest concentrations in the 1-3 km layer, and O_3 (peak value >3km) are the exceptions. The model performed best in the lower altitudes, and for primary emitted species such as CO, ethane, propane, NO_2, NO, and toluene. All species with the exception of SO_2 and xylene are predicted within a factor of 2, and many within a factor of 1.2. The correlation coefficients for all the listed species are greater than 0.67. The predictions for the 1-3 km region for SO_2, O_3, NO_z are usually better than the <1km layer values in terms of mean values reflecting the fact that this layer is not

so heavily impacted by the very local sources. However R-values are lower. The predictions >3km are markedly poorer, with R-values typically lower than 0.5. J-values are a notable exception, and are predicted with appreciable skill at all altitudes. J-value predictions mainly reflected the simulations for aerosol optical properties and clouds. J[NO_2] is very sensitive to fractional cloud, and the correlation coefficients for it are relatively low compared to predictions for other J-values.

The values presented in Table 3 are a mixture of North American and Asian emission influenced air masses. To further evaluate the model performance the data was stratified using model-calculated Asian ratios. The statistics for data points with Asian ratios <20% and >80% are presented in Tables 4 and 5, respectively. At altitudes below 1 km, the model performance for air masses with Asian ratio < 20% was better than that with Asian ratio > 80%, as represented by the R values for emitted short-lived species, such as SO_2, NO, NO_2, and their products HNO_3, NO_z, and NO_y. This decrease in performance with distance from the emission source areas is due to the accumulation of errors in the transport, chemistry and removal processes. This performance difference for emitted short-lived species also existed at the altitude 1-3km, but not as significant as that below 1km. At altitudes above 3km, the model did not show any systematic differences between the high and low Asian-impact data sets.

Further insights into the model performance are shown in Figure 12, where the observed and calculated CO distributions are presented. The observed CO distribution shows a high degree of variability with values of CO > 160 ppbv found at all altitudes. The highest values however were found below 2km around LA. The model shows the same basic behavior and is able to accurately capture the mean behavior (as shown in Table 3 where the model mean values are within 6% of the observations at all altitudes). The distribution of the bias (simulated-observed) is presented in Figure 12c. The estimated VOC age is shown in Figure 12d, and reveals that aged air is found at all attitudes and latitudes. No simple relationship appears between CO bias and air mass age. Similar results are found for observed and modeled NO_y.

8. Trinidad Head Surface Site

During the ITCT-2K2 experiment extensive measurements were also performed at the Trinidad Head ground station (41.05N, 124.15W) located on the coast of Northern California (Figure 1). The regional model was also used to provide forecast support and post-analysis interpretation to the surface observations. Figure 13 shows the model simulations compared to the surface measurements from Julian day 110 to 143 (April 10 to May 13). Figure 13a shows that simulated wind speeds agreed with the observed diurnal peak wind velocities, and reflected their daily variation trend. However, due to the relatively coarse resolution the RAMS prediction failed to represent the nighttime calm winds at Trinidad Head. Both the RAMS prediction and the observations showed that north and northeast winds prevailed (Figure 13b). The simulated CO and NO_y concentrations are consistent with the observation as shown in Figures 13c and 13d. Both the observed and the simulated values show that CO and NO_y are generally correlated. These two plots also show the CFORS simulated anthropogenic CO Asian ratio and NO_x age. In general CO Asian ratios >0.5 are associated with air masses older than 50 hours. The highest NO_y values occurred for air masses older than ~50 hours. For example the CO and NO_y peak concentrations on Julian day 113, 119-120 and 132 were associated with low surface wind speeds, implying that these peaks were mainly due to the accumulation of pollutants emitted from surrounding sources and transported to Trinidad Head under the low-wind speed situations.

Further insights into the role of local emission sources on Trinidad head is found in Figure 13e, where the simulated and observed propane, CFORS simulated VOC age, and observed methyl-t-butyl ether (MTBE), a compound mainly used in North America, are plotted. As shown the simulation results accurately capture the observed propane features. MTBE is a good tracer for local sources, as shown by its plume-like structure (Goldstein et al., this issue; Millet et al., this issue). The MTBE peaks correlate with peaks in propane (and other pollutants), but propane shows broader maxima, reflecting the longer

lifetime of propane. The simulated VOC age shows clearly a reversed variation with observed MTBE, providing further evidence for the utility of the VOC age indicator in helping to identify local and distant sources. As shown by the CO results in Figure 13c, the fresh pollution events at Trinidad Head are superimposed on air that is a mixture of Asian and American sources.

Both observed and simulated CO and propane show a clear declining trend during this one-month period (Figures 13c and 13e). The CO background concentration declined from 150 ppbv in April to 125 ppbv in May, while the propane background concentration declined from 0.3 to 0.15 ppbv. This seasonal variation trend reflects the increased CO and VOC consumptions by OH as the sunshine time became longer and photochemical reactions became more active (simulated daytime OH increased by about 30% during this period).

There were two instruments measuring aerosol ions at Trinidad Head: PILS (particle-into-liquid sampler) and the aerodyne AMS (Aerosol Mass Spectrometer, Allan et al., this issue). Both of these instruments report a cut-off diameter of ~1μm to capture submicron ions. The measured and simulated aerosol sulfate, nitrate and ammonium concentrations are presented in Figures 13f, 13g and 13h, respectively. As discussed in Allan et al. (this issue), the AMS instrument observed consistently more nitrate than the PILS instrument. This may be due to the presence of organic nitrates and/or amines. The simulated nitrate values are shown in Figure 13g for <1μm and <2.5μm diameters. The model results show an appreciable amount of nitrate in particles with diameters between 1μm to 2.5μm. The simulation curves for <1μm and <2.5μm tend to encompass most of the observed nitrate, suggesting that differences in inlet cut-offs could account for some of the differences between the measurements. In fact, the AMS 1μm cut-off diameter was not absolute, and the measurements included some particles between 1 and 2μm. A second AMS instrument configured to study size resolved aerosol composition did identify sub- as well as super-micron nitrate, with the super-micron nitrate associated with sea salt particles. The sea salt mode is mainly

in the super-micron regime but the tail did go down into the submicron. The simulated fraction of nitrate in the super-micron particles varied from 5% to ~100%, with a mean value of 30%, and with the super micron fraction dominating under elevated sea salt conditions. Sea salt nitrate was also linked to a suppression of chloride relative to sodium in the PILS observations as well as in the simulations.

The simulated and observed ammonium values are shown in Figure 13h. The AMS and PILS measurements quantitatively agree (slope AMS versus PILS of 1.099, with r^2 of 0.58, Allan et al., this issue)). The model predictions are generally consistent with the observations, with essentially all of the ammonium in the particles below < 1μm, which was also verified by the AMS size-resolved measurements. Our prediction overestimated fine sea salt. After we removing this overestimation, ammonium prediction looks reasonable (Figure 13h).

9. Conclusion

In this paper a multi-scale modeling system comprised of a regional tracer model, regional chemical transport model with a nested grid, and with lateral boundary conditions from the global model MOZART, was used to analyze aircraft and surface observations obtained during the ITCT-2K2 experiment. This model system was shown to have substantive predictive capability for the region and times of the NOAA WP-3 flights during the ITCT-2K2 experiment.

The model estimated air mass source and chemical age indicators were used to help analyze the observations. The Asian air masses were found to have lower ΔAcetone/ΔCO, ΔMethanol/ΔCO, and ΔPropane/ΔEthyne ratios than air masses impacted by American sources. During the long-distance transport Asian air masses experienced significant NO_y losses, associated with gas-aerosol interaction and removal processes. The VOC and NO_x age analysis indicated that air masses measured had chemical ages ranging from <0.5 to > 10 days. Asian air masses were usually aged (> 5 days). CO and O_3 were found to

have net negative budgets in the places dominated by Asian influences, with CO losses due to reaction with OH, and O_3 lost via photolytic dissociation. In the MBL OH levels were elevated and CO destruction was high. CO and O_3 chemical net budgets turned positive in polluted American air masses.

The aerosol partitioning of nitrate was shown to be important. Without aerosol consideration, the model overestimated HNO_3, especially for its background concentration along the U.S west coast. This result also implies that NO_y should decrease because of this process during the trans-Pacific transport.

Several big cities exist along the US west coast. This study indicated that these cities received little Asian influence, and that photochemical processes were dominated by local sources. At Trinidad Head, most high concentrations of pollutants are associated with calm-wind scenarios, and the accumulation of local sources. Seasonal variations of CO and VOCs showed a clear declining trend from April to May at this site. The high-resolution nested simulation greatly improved the prediction for emitted and secondary-generated species. The resolution change affected not only the emission intensity and distribution, but also the associated photochemical behavior. In the coarse resolution (60km) mode the concentrations of primary emitted species were underestimated, O_3 production was widespread, and the titrating effect of high-concentrated pollutants was not resolved. This resulted in an overestimation of O_3, NO_z and OH. The nesting simulation significantly improved the model performance.

The multi-scale modeling system consisting of nested models was shown to provide a viable tool for studying trans-Pacific transport, and the results were often consistent with observations. However, the difference between the simulations and measurements indicate that further improvements are needed to better quantify multi-scale and multi-source problems.

Acknowledgement:

This work was supported primarily by the NOAA Atmospheric Chemistry Program (Grant No. NA16GP2315). Partial support was provided by the NSF Atmospheric Chemistry Program (NSF grant Atm-0002698), NASA GTE and ACMAP programs, and the Department of Energy Atmospheric Chemistry Program. This work (I. Uno) was also partly supported by Research and Development Applying Advanced Computational Science and Technology (ACT-JST) and the CREST of Japan Science and Technology Corporation. Special thanks go to Gerhard Hübler, Michael Trainer and Fred Fehsenfeld for the efforts in the organization and execution of the ITCT-2K2 experiment. We also acknowledge the use of data collected by Joost de Gouw, J. Andy Neuman, David. D. Parrish, Thomas B. Ryerson and their colleagues.

Reference:

Allan, J. D., K. N. Bower, H. Coe, H. Boudries, J. T. Jayne, M. R. Canagaratna, D. B. Millet, Allen H. Goldstein, P. K. Quinn, R. J. Weber and D. R. Worsnop, Submicron aerosol composition at Trinidad Head, CA, during ITCT 2K2, its relationship with gas phase volatile organic carbon and assessment of instrument performance. submitted to *J. Geophys. Res.*, this issue.

Carmichael, G. R., Y. Tang, G. Kurata, I. Uno, D. G. Streets, J.-H. Woo, H. Huang, J. Yienger, B. Lefer, R. E. Shetter, D. R. Blake, A. Fried, E. Apel, F. Eisele, C. Cantrell, M. A. Avery, J. D. Barrick, G.W. Sachse, W. L. Brune, S. T. Sandholm, Y. Kondo, H. B. Singh, R. W. Talbot, A. Bandy, A. D. Clarke, and B. G. Heikes, Regional-Scale chemical transport modeling in support of intensive field experiments: overview and analysis of the TRACE-P Observations, *J. Geophys. Res.*, *108(D21), 8823,* doi: *10.1029/2002JD003117*, 2003a.

Carter, W., Documentation of the SAPRC-99 chemical mechanism for voc reactivity assessment, Final Report to California Air Resources Board Contract No. 92-329, University of California-Riverside, May 8, 2000.

Cooper, O.R., et al., A case study of trans-Pacific warm conveyor belt transport: The influence of merging airstreams on trace gas import to North America, *J. Geophys. Res.*, this issue.

Corbett, J. J., P. S. Fischbeck, S. N. Pandis, Global Nitrogen and Sulfur Emissions Inventories for Oceangoing Ships, *J. Geophys. Res., 104 (D3), 3457-3470*, 1999.

Garratt, J. R., The Internal Boundary Layer – A Review, *Boundary-Layer Meteorol.* **5**0, 171–203, 1990.

de Gouw, J. A., O. R. Cooper, C. Warneke, P. K. Hudson, C. A. Brock, F. C. Fehsenfeld, J. S. Holloway, G. Hübler, D. M. Murphy, J. B. Nowak, D. D. Parrish, T. B. Ryerson, and M. Trainer, Chemical composition of air pollution transported from Asia to the U.S. west coast during ITCT2k2: fossil fuel versus biomass burning signatures, submitted to *J. Geophys. Res.*, this issue.

Goldstein, A. H., D. B. Millet, M. McKay, L. Jaegle, L. W. Horowitz, O. Cooper, D. D. Parrish, R. Hudman, D. J. Jacob, S. Oltmans, A. Clark, Impact of Asian Emissions on Observations at Trinidad Head, California, during ITCT 2K2, submitted to *J. Geophys. Res.*, this issue.

Guenther, A., C. N. Hewitt, D. Erickson, R. Fall, C. Geron, T. Graedel, P. Harley, L. Klinger, M. Lerdau, W. A. McKay, T. Pierce, B. Scholes, R. Steinbrecher, R. Tallamraju, J. Taylor and P. Zimmerman, A global-model of natural volatile organic-compound emissions, *J. Geophys. Res., 100 (D5), 8873-8892,* 1995.

Jacob, D. J., J. A. Logan, P. P. Murti, Effect of rising Asian emissions on surface ozone in the United States, *Geophys. Res. Lett.*, 26 (14), 2175-2178, 1999.

Jacob, D. J., J. H. Crawford, M. M. Kleb, V. E. Conners, R. J. Bendura, J. L. Raper, Jr., G. W. Sachse, J. C. Gille and L. Emmons, The TRAnsport and Chemical Evolution over the Pacific (TRACE-P) mission: Design, execution, and overview of results, *J. Geophys. Res., TRACE-P issue,* 2003.

Jaffe, D., T. Anderson, D. Covert, R. Kotchenruther, B. Trost, J. Danielson, W. Simpson, T. Berntsen, S. Karlsdottir, D. Blake, J. Harris, G. R. Carmichael, and I. Uno, Transport of Asian air pollution to North America, *Geophys. Res. Lett.*, *26*, 711-714, 1999.

Jaffe, D., I. McKendry, T. Anderson, and H. Price, Six 'new' episodes of trans-Pacific transport of air pollutants, Atmos. Environ., 37 (3), 391-404, 2003.

Kim Y. P., J. H. Seinfeld, and P. Saxena, Atmospheric gas-aerosol equilibrium I: Thermodynamic model, *Aerosol Sci. Technol.*, 19, 151-181, 1993a.

Kim Y. P., J. H. Seinfeld, and P. Saxena, Atmospheric gas-aerosol equilibrium II: Analysis of common approximations and activity coefficient calculation methods, *Aerosol Sci. Technol.*, 19, 182-198, 1993b.

Kim Y. P., and J. H. Seinfeld, Atmospheric gas-aerosol equilibrium III: Thermodynamics of crustal elements Ca^{2+}, K^{+}, Mg^{2+}, *Aerosol Sci. Technol.*, 22, 93-110, 1995.

Kotchenruther, R. A., D. A. Jaffe, H. J. Beine, T. L. Anderson, J. W. Bottenheim, J. M. Harris, D. R. Blake, and R. Schmitt, Observations of ozone and related species in the northeast Pacific during the PHOBEA campaigns: 2. Airborne observations, *J. Geophys. Res.*, *106(D7)*, 7463-7483, 2001.

Horowitz, L.W., S. Walters, D. L. Mauzerall, L. K. Emmons, P. J. Rasch, C. Granier, X. X. Tie, J.-F. Lamarque, M. G. Schultz, G. S. Tyndall, J. J. Orlando, and G. P. Brasseur, A global simulation of tropospheric ozone and related tracers: Description and evaluation of MOZART, version 2, *J. Geophys. Res., 108(D24), 4784, doi:10.1029/2002JD002853, 2003.*

Olivier, J. G. J., A. F. Bouwman, C. W. M. Van der Maas, J. J. M. Berdowski, J. P. J. Bloos, A. J. H. Visschedijk, P. Y. J. Zandveld and J. L. Haverlag, Description of EDGAR Version 2.0.: A set of global emission inventories of greenhouse gases and ozone-depleting substances for all anthropogenic and most natural sources on a per country basis and on 1ºx1º grid. RIVM/TNO report nr. 771060002, Bilthoven, 1996.

Kuhns, H., Big Bend Regional Aerosol and Visibility Observational (BRAVO) Study Modeling Emissions Inventory, Desert Research Institute (DRI) Report, 2001.

Langmann, B., S. E. Bauer, and I. Bey, The influence of the global photochemical composition of the troposphere on European summer smog, Part I: Application of a global to mesoscale model chain, *J. Geophys. Res.,* 108 (D4), 4146, doi:10.1029/2002JD002072, 2003.

Madronich, S. and S. Flocke, The role of solar radiation in atmospheric chemistry, in Handbook of Environmental Chemistry (P. Boule, ed.), Springer-Verlag, Heidelberg, 1-26, 1999.

Millet, D. B., A. H. Goldstein, J. D. Allan, T. S. Bates, H. Boudries, K. N. Bower, H. Coe, Y. Ma, M. McKay, P. K. Quinn, A. Sullivan, R. J. Weber, and D. R. Worsnop, VOC measurements at Trinidad Head, CA during ITCT 2K2: Analysis of sources, atmospheric composition and aerosol residence times, submitted to *J. Geophys. Res.*, this issue.

Neuman, J. A., J. D. Nowak, C. A. Brock, M. Trainer, F. C. Fehsenfeld, J. S. Holloway, G. Hübler, P. K. Hudson, D. M. Murphy, D. K. Nicks Jr., D. Orsini, D. D. Parrish, T. B. Ryerson, D. T. Sueper, A. Sullivan, and R. Weber, Variability in ammonium nitrate formation and nitric acid depletion with altitude and location over California, *J. Geophys. Res. 108, D17, 4557, doi:10.1029/2003JD003616, 2003.*

Pickering, K. E., Y. S. Wang, W. K. Tao, C. Price, J. F. Muller, Vertical distributions of lightning NOx for use in regional and global chemical transport models, *J. Geophys. Res., 103 (D23), 31203-31216*, 1998.

Pielke, R. A., W. R. Cotton, R. L. Walko, C. J. Tremback, W.A. Lyons, L.D. Grasso, M.E. Nicholls, M.D.Moran, D.A. Wesley, T.J. Lee and J.H. Copeland, A comprehensive meteorological modeling system -RAMS, *Meteorol. Atmos. Phys*., 49, 69-91, 1992.

Strahan, S. E., Climatologies of lower stratospheric NO_y and O_3 and correlations with N_2O based on in situ observations, *J. Geophys. Res., 104 (D23), 30463-30480*, 1999.

Streets, D. G., T.C. Bond, G. R. Carmichael, S. D. Fernandes, Q. Fu, D. He, Z. Klimont, S. M. Nelson, N. Y. Tsai, M. Q. Wang, J.-H. Woo, and K. F. Yarber, A year-2000 inventory of gaseous and primary aerosol emissions in Asia to support TRACE-P modeling and analysis. *J. Geophys. Res., 108(D21), 8809, doi:10.1029/2002JD003093, 2003a.*

Streets D.G, K.F. Yarber, J.-H. Woo, and G.R. Carmichael, Biomass burning in Asia: annual and seasonal estimates and atmospheric emissions, *Global Biogeochemical Cycles, doi:10.1029/2003GB002040, 2003b.*

Tang, Y., A case study of nesting simulation for the Southern Oxidants Study 1999 at Nashville. *Atmos. Environ.*, 36(10), 1691-1705, 2002.

Tang, Y., G. R. Carmichael, I. Uno, J.-H. Woo, G. Kurata, B. Lefer, R. E. Shetter, H. Huang, B. E. Anderson, M. A. Avery, A. D. Clarke and D. R. Blake, Impacts of aerosols and clouds on photolysis frequencies and photochemistry during TRACE-P, part II: three-dimensional study using a regional chemical transport model, *J. Geophys. Res., 108(D21), 8822, doi: 10.1029/2002JD003100*, 2003a.

Tang, Y., G. R. Carmichael, J.-H. Woo, N. Thongboonchoo, G. Kurata, I. Uno, D. G. Streets, D. R. Blake, R. J. Weber, R. W. Talbot, Y. Kondo and H. B. Singh, the influences of biomass burning during TRACE-P experiment identified by the regional chemical transport model, *J. Geophys. Res.*, *108(D21), 8824,* doi: *10.1029/2002JD003110*, 2003b.

Tang Y., G. R. Carmichael, J. H. Seinfeld, D. Dabdub, Rodney J. Weber, B. Huebert, A. D. Clarke, S. A. Guazzotti, D. A. Sodeman, K. A. Prather, I. Uno, J.-H. Woo, D. G. Streets, P. K. Quinn, J. E. Johnson, C.-H. Song, A. Sandu**,** R. W. Talbot and J. E. Dibb, three-dimensional simulations of inorganic aerosol distributions in East Asia during spring 2001, *J. Geophys. Res.*, doi: *10.1029/2003JD004201, ACE-Asia issue II*, 2004.

Trainer, M., D. D. Parrish, M. P. Buhr, R. B. Norton, F. C. Fehsenfeld, K. G. Anlauf, J. W. Bottenheim, Y. Z. Tang, H. A. Wiebe, J. M. Roberts, R. L. Tanner, L. Newman, V. C. Bowersox, J. F. Meagher, K. J. Olszyna, M. O. Rodgers, T. Wang, H. Berresheim, K. L. Demerjian and U. K. Roychowdhury, Correlation of ozone with NOy in photochemical aged air. *J. Geophy. Res., 98(D2)*, *2917-2925,* 1993.

Uno, I., H. Amano, S. Emori, K. Kinoshita, I. Matsui, N. Sugimoto, Trans-Pacific yellow sand transport observed in April 1998: A numerical simulation, *J. Geophys. Res.*, 106 (D16), 18331-18344, 2001.

Uno, I., G. R. Carmicahel, D.G. Streets, Y. Tang, J. J. Yienger, S. Satake, Z. Wang, J.-H. Woo, S. Guttikunda, M.Uematsu, K. Matsumoto, H. Tanimoto, K. Yoshioka and T. Iida, Regional chemical weather forecasting system CFORS: model descriptions and analysis of surface observations at Japanese island stations during the ACE-Asia experiment. *J. Geophys. Res.*, 108 (D23), 8668, *doi: 10.1029/2002JD002845*, 2003.

VanCuren R. A., and T. A. Cahill, Asian aerosols in North America: frequency and concentration of fine dust, *J. Geophy. Res.,* 107 (D24), doi: 10.1029/2002JD002204, 2002.

Woo, J.-H., D. G. Streets, G. R.Carmichael, Y. Tang, B.-I. Yoo, W.-C. Lee, N. Thongboonchoo, S. Pinnock, G. Kurata, and I. Uno, Biomass and Biofuel Emissions and Their Impact on Trace Gas Distributions in Asia during the TRACE-P Experiment**,** *J. Geophys. Res., 108(D21), 8812, doi:10.1029/2002JD003200,* 2003.

Yienger, J. J., M. Galanter, T. A. Holloway, M. J. Phadnis, S. K. Guttikunda, G. R. Carmichael, W. J. Moxim, and H. Levy, The episodic nature of air pollution transport from Asia to North America, *J. Geophys. Res.,*105 (D22), 26931-26945, 2000.

Table 1. The 17 vertical layers (over sea surface) used in CFORS and STEM-2K3 and CO background profile in the Eastern Pacific

Altitude(km)	0.075	0.24	0.44	0.68	0.96	1.3	1.7	2.2	2.8	3.5	4.4	5.4	6.6	8.1	9.8	11.6	13.4
CO (ppbv)	120	120	120	120	120	120	120	110	110	110	110	108	105	105	98	85	80

Table 2. Reaction index as mentioned in Figure 6

Reaction Index #	Reaction Equations
2	$O^3P + O_2 \rightarrow O_3$
7	$O_3 + NO \rightarrow NO_2 + O_2$
17	$O_3 + hv \rightarrow O_2 + O^3P$
18	$O_3 + hv \rightarrow O_2 + O^1D$
19	$O^1D + H_2O \rightarrow 2OH$
21	$OH + NO \rightarrow HONO$
22	$HONO + hv \rightarrow OH + NO$
25	$OH + NO_2 \rightarrow HNO_3$
29	$OH + CO + O_2 \rightarrow HO_2 + CO_2$
30	$OH + O_3 \rightarrow HO_2 + O_2$
31	$HO_2 + NO \rightarrow NO_2 + OH$
32	$HO_2 + NO_2 \rightarrow HNO_4$
33	$HNO_4 + hv \rightarrow 0.61HO_2 + 0.61NO_2 + 0.39OH + 0.39NO_3$
36	$HO_2 + O_3 \rightarrow OH + 2O_2$
37	$HO_2 + HO_2 \rightarrow H_2O_2 + O_2$
38	$HO_2 + HO_2 + H_2O \rightarrow H_2O_2 + O_2 + H_2O$
41	$H_2O_2 + hv \rightarrow 2OH$
42	$H_2O_2 + OH \rightarrow HO_2 + H_2O$
43	$HO_2 + OH \rightarrow O_2 + H_2O$
44	$OH + SO_2 + H_2O + O_2 \rightarrow H_2SO_4 + HO_2$
45	$H_2 + OH \rightarrow HO_2$
46	$CH_3O_2 + NO + O_2 \rightarrow NO_2 + HCHO + HO_2$
51	$RO_2_R + NO \rightarrow NO_2 + HO_2$
123	$HCHO + hv + 2O_2 \rightarrow 2HO_2 + CO$
124	$HCHO + hv \rightarrow CO + H_2$
125	$OH + HCHO \rightarrow HO_2 + CO$
126	$HCHO + HO_2 \rightarrow HOCOO$
127	$HOCOO \rightarrow HCHO + HO_2$
130	$CH_3CHO + OH \rightarrow CCO_O_2$
131	$CH_3CHO + hv \rightarrow CO + HO_2 + CH_3O_2$
133	$RCHO + OH \rightarrow 0.034CO + 0.034CH_3CHO + Other$
134	$RCHO + hv \rightarrow CH_3CHO + CO + HO_2 + RO_2_R$
200	$C_2H_2 + OH \rightarrow 0.603OH + 0.297HO_2 + 0.393CO + 0.1RO_2_R + 0.096HCHO$

*RCHO is lumped aldehydes with three and more carbons, RO_2_R is peroxy radical operator representing NO to NO_2 conversion with HO_2 formation, and CCO_O_2 represents acetyl peroxy radicals (Carter, 2000)

Table 3. Observed and Simulated (60 km resolution) Mean Values and Their Correlation Coefficients (R) for ITCT-2K2 all WP-3 flights

Species and Variables	Below 1km			1km to 3km			Above 3km		
	Observed	Modeled	R	Observed	Modeled	R	Observed	Modeled	R
Pressure (hPa)	971.5	963.1	0.96	801.2	798.5	0.99	554.4	551.7	0.99
Wind Speed (m/s)	8.2	8.4	0.67	8.0	7.3	0.68	12.7	11.5	0.88
Relative Humidity (%)	68.8	58.3	0.82	28.8	33.9	0.85	27.5	28.2	0.73
CO (ppbv)	154	163	0.92	135	147	0.60	120	113	0.18
O_3 (ppbv)	47.2	58.1	0.81	57.3	57.8	0.66	59.8	64.0	0.47
Ethane (ppbv)	1.62	1.52	0.82	1.31	1.15	0.22	0.98	0.77	0.40
Propane (ppbv)	0.60	0.36	0.83	0.32	0.22	0.34	0.13	0.06	0.30
Ethyne (ppbv)	0.33	0.34	0.86	0.23	0.23	0.47	0.16	0.11	0.14
SO_2 (ppbv)	0.76	0.23	0.52	0.44	0.35	0.41	0.30	0.10	0.18
Acetone (ppbv)	1.03	0.71	0.89	1.20	0.55	0.64	0.89	0.27	0.28
PAN (ppbv)	0.16	0.57	0.68	0.44	0.47	0.06	0.14	0.15	0.26
NO_2 (ppbv)	1.76	1.04	0.88	0.58	0.49	0.65	0.055	0.018	0.43
NO (ppbv)	0.52	0.31	0.83	0.15	0.13	0.69	0.019	0.009	0.43
HNO_3 (ppbv)	0.80	0.65	0.87	0.81	0.64	0.73	0.13	0.12	0.60
NO_y (ppbv)	3.3	3.8	0.92	1.75	2.54	0.66	0.42	0.42	0.51
NO_z (ppbv)	1.64	2.46	0.95	1.25	1.92	0.66	0.38	0.40	0.57
Toluene (ppbv)*	0.113	0.102	0.91	0.0492	0.0604	0.69	0.019	0.017	0.18
Xylene (ppbv)*	0.150	0.051	0.85	0.0279	0.0195	0.73	0.0047	0.0035	0.20
$J[NO_2]$ (1/s)	6.66×10^{-3}	7.62×10^{-3}	0.67	9.1×10^{-3}	8.83×10^{-3}	0.58	0.010	0.0092	0.56
$J[O_3\rightarrow O_2+O^1D]$ (1/s)	2.00×10^{-5}	2.30×10^{-5}	0.86	2.92×10^{-5}	2.77×10^{-5}	0.84	2.95×10^{-5}	2.77×10^{-5}	0.83
$J[H_2O_2]$ (1/s)	4.31×10^{-6}	5.75×10^{-6}	0.79	6.21×10^{-6}	6.88×10^{-6}	0.74	6.72×10^{-6}	7.10×10^{-6}	0.77
$J[HNO_3]$ (1/s)	3.67×10^{-7}	4.94×10^{-7}	0.84	5.34×10^{-7}	5.93×10^{-7}	0.81	5.47×10^{-7}	5.90×10^{-7}	0.83
$J[HNO_2\rightarrow OH+NO]$ (1/s)	1.46×10^{-3}	1.49×10^{-3}	0.68	2.02×10^{-3}	1.73×10^{-3}	0.60	2.26×10^{-3}	1.81×10^{-3}	0.59
$J[HCHO\rightarrow H+HCO]$ (1/s)	1.87×10^{-5}	2.49×10^{-5}	0.81	2.75×10^{-5}	3.05×10^{-5}	0.77	3.20×10^{-5}	3.37×10^{-5}	0.79
$J[HCHO\rightarrow H_2+CO]$ (1/s)	3.13×10^{-5}	3.58×10^{-5}	0.74	4.65×10^{-5}	4.33×10^{-5}	0.69	5.58×10^{-5}	4.70×10^{-5}	0.69

* measured with proton-transfer-reaction mass spectrometry (PTR-MS).

Table 4. Observed and Simulated (60 km resolution) Mean Values and Their Correlation Coefficients (R) for ITCT-2K2 WP-3 flights with CO Asian Ratio < 20%

Species and Variables	Below 1km			1km to 3km			Above 3km		
	Observed	Modeled	R	Observed	Modeled	R	Observed	Modeled	R
CO (ppbv)	172	196	0.91	146	177	0.60	110	119	0.37
O_3 (ppbv)	51.8	71.6	0.81	61.8	67.8	0.71	50. 2	54.3	0.54
Ethane (ppbv)	1.86	1.90	0.82	1.43	1.41	0.16	0.93	0.73	0.27
Propane (ppbv)	0.89	0.54	0.83	0.51	0.35	0.27	0.21	0.09	0.26
Ethyne (ppbv)	0.45	0.41	0.87	0.28	0.27	0.46	0.18	0.09	0.22
SO_2 (ppbv)	1.16	0.40	0.48	0.70	0.64	0.31	0.26	0.16	-0.02
Acetone (ppbv)	1.42	0.91	0.89	1.53	0.73	0.56	0.99	0.34	0.35
PAN (ppbv)	0.23	0.96	0.60	0.79	0.85	-0.10	0.12	0.25	0.40
NO_2 (ppbv)	2.65	1.90	0.88	1.15	1.01	0.61	0.17	0.10	0.34
NO (ppbv)	0.89	0.57	0.82	0.31	0.27	0.65	0.06	0.04	0.35
HNO_3 (ppbv)	1.39	1.17	0.86	1.58	1.28	0.68	0.33	0.36	0.73
NO_y (ppbv)	5.45	6.78	0.92	3.38	4.98	0.61	0.78	1.11	0.47
NO_z (ppbv)	2.40	4.31	0.95	2.13	3.69	0.60	0.61	0.98	0.56
Toluene (ppbv)	0.156	0.174	0.91	0.069	0.109	0.67	0.029	0.017	0.25
Xylene (ppbv)	0.165	0.091	0.84	0.034	0.039	0.72	0.004	0.003	0.26
$J[NO_2]$ (1/s)	6.53×10^{-3}	6.90×10^{-3}	0.93	8.11×10^{-3}	7.86×10^{-3}	0.44	0.0084	0.0050	0.65
$J[O_3\rightarrow O_2+O^1D]$ (1/s)	2.11×10^{-5}	2.07×10^{-5}	0.98	2.78×10^{-5}	2.29×10^{-5}	0.92	3.22×10^{-5}	1.38×10^{-5}	0.96
$J[H_2O_2]$ (1/s)	4.31×10^{-6}	5.21×10^{-6}	0.97	5.61×10^{-6}	5.99×10^{-6}	0.68	6.08×10^{-6}	3.71×10^{-6}	0.89
$J[HNO_3]$ (1/s)	3.77×10^{-7}	4.47×10^{-7}	0.98	4.96×10^{-7}	5.08×10^{-7}	0.84	5.53×10^{-7}	3.05×10^{-7}	0.94
$J[HNO_2\rightarrow OH+NO]$ (1/s)	1.43×10^{-3}	1.34×10^{-3}	0.94	1.79×10^{-3}	1.53×10^{-3}	0.46	1.88×10^{-3}	0.98×10^{-3}	0.68
$J[HCHO\rightarrow H+HCO]$ (1/s)	1.86×10^{-5}	2.22×10^{-5}	0.98	2.45×10^{-5}	2.58×10^{-5}	0.72	2.76×10^{-5}	1.68×10^{-5}	0.90
$J[HCHO\rightarrow H_2+CO]$ (1/s)	3.11×10^{-5}	3.23×10^{-5}	0.96	4.13×10^{-5}	3.74×10^{-5}	0.58	4.57×10^{-5}	2.43×10^{-5}	0.79

Table 5. Observed and Simulated (60 km resolution) Mean Values and Their Correlation Coefficients (R) for ITCT-2K2 WP-3 flights with CO Asian Ratio > 80%

Species and Variables	Below 1km			1km to 3km			Above 3km		
	Observed	Modeled	R	Observed	Modeled	R	Observed	Modeled	R
CO (ppbv)	129	121	0.90	127	118	0.46	125	112	0.085
O_3 (ppbv)	40.7	38.1	0.74	53.2	47.5	0.31	64.4	66.9	0.46
Ethane (ppbv)	1.29	0.97	0.95	1.23	0.86	0.73	1.03	0.77	0.44
Propane (ppbv)	0.20	0.11	0.97	0.18	0.08	0.87	0.13	0.06	0.33
Ethyne (ppbv)	0.20	0.23	0.85	0.19	0.17	0.64	0.17	0.11	0.17
SO_2 (ppbv)	0.21	0.021	-0.02	0.21	0.09	0.35	0.32	0.11	0.26
Acetone (ppbv)	0.48	0.43	0.77	0.86	0.35	-0.18	0.92	0.25	0.18
PAN (ppbv)	0.060	0.075	0.77	0.089	0.094	0.76	0.15	0.14	0.33
NO_2 (ppbv)	0.25	0.020	0.12	0.035	0.011	-0.01	0.026	0.006	0.30
NO (ppbv)	0.074	0.008	0.28	0.011	0.006	0.19	0.008	0.005	0.18
HNO_3 (ppbv)	0.077	0.058	-0.35	0.070	0.053	0.28	0.058	0.069	0.25
NO_y (ppbv)	0.40	0.24	0.30	0.30	0.23	0.38	0.34	0.29	0.31
NO_z (ppbv)	0.23	0.21	0.007	0.26	0.22	0.53	0.34	0.28	0.31
$J[NO_2]$ (1/s)	7.53×10^{-3}	9.23×10^{-3}	0.31	9.88×10^{-3}	1.03×10^{-2}	0.61	0.0101	0.0104	0.63
$J[O_3\rightarrow O_2+O^1D]$ (1/s)	1.89×10^{-5}	3.02×10^{-5}	0.72	3.23×10^{-5}	3.59×10^{-5}	0.81	2.88×10^{-5}	3.34×10^{-5}	0.83
$J[H_2O_2]$ (1/s)	4.63×10^{-6}	7.13×10^{-6}	0.54	6.82×10^{-6}	8.30×10^{-6}	0.75	6.70×10^{-6}	8.22×10^{-6}	0.83
$J[HNO_3]$ (1/s)	3.70×10^{-7}	6.26×10^{-7}	0.66	5.87×10^{-7}	7.33×10^{-7}	0.80	5.40×10^{-7}	6.94×10^{-7}	0.85
$J[HNO_2\rightarrow OH+NO]$ (1/s)	1.65×10^{-3}	1.80×10^{-3}	0.34	2.20×10^{-3}	2.02×10^{-3}	0.62	2.25×10^{-3}	2.06×10^{-3}	0.66
$J[HCHO\rightarrow H+HCO]$ (1/s)	2.00×10^{-5}	3.16×10^{-5}	0.59	3.07×10^{-5}	3.78×10^{-5}	0.76	3.20×10^{-5}	3.94×10^{-5}	0.84
$J[HCHO\rightarrow H_2+CO]$ (1/s)	3.45×10^{-5}	4.45×10^{-5}	0.47	5.12×10^{-5}	5.21×10^{-5}	0.70	5.60×10^{-5}	5.42×10^{-5}	0.76

Figure Captions

Figure 1. Model domains, NOAA WP-3 flight paths (colored lines), and estimated CO emissions on the various domains.

Figure 2. ITCT aircraft-observed correlations (left panels) classified by simulated Asian Ratio < 20% and > 80%, and TRACE-P aircraft measured correlations (right panels). All plots are marked with linear fit lines and correlation coefficient R.

Figure 3. Observed ratios versus VOC age and NO_x age estimated by the CFORS model for all ITCT flights, color-coded by VOC age.

Figure 4. Simulated results at 21:00GMT, April 25, 2002. CO Asian ratios are presented in contour line in plots a and b. CO and O_3 budgets are in ppbv/hr.

Figure 5. STEM simulations compared to measurements for the WP-3 flight on April 25.

Figure 6. Simulated species budgets and their components for O_3, CO, OH, HO_2 and HCHO at 19:00 GMT (altitude 2837m), 19:03 GMT (altitude 3630m), and 21:00 GMT (altitude 470m) along the WP-3 flight path on April 25. Some net budgets, concentrations, and rate terms are multiplied a factor of 10 for display purposes. Negative values represent loss terms. For each term, the bar sequence from left to right is 19:00 GMT, 19:03 GMT, and 21:00 GMT. The reaction index (R#) is listed in Table 2.

Figure 7. Simulated results at 21:00GMT, May 15, 2002. CO Asian ratios are presented by contour line in panels a and b.

Figure 8. STEM simulations compared to measurements for the WP-3 flight on May 15.

Figure 9. STEM simulations with and without the aerosol consideration compared to observations of 4 WP-3 flights, whose paths are shown by the plot e.

Figure 10. Coarse (60km resolution) and nested (12 km resolution) simulated CO and O_3 at 400m at 21GMT, May 13, for the WP-3 flight 10 over Los Angeles and surrounding area.

Figure 11. Simulations compared to the measurements along the path of WP-3 flight 10 shown in Figure 12c. The nested and coarse simulations have similar J-value predictions. So plots g and h show only one simulation.

Figure 12. Latitude-Altitude distributions of CO, CO difference, VOC age, NO_y, and NO_y difference for All WP-3 flights.

Figure 13. Simulation compared to surface observations at Trinidad Head.

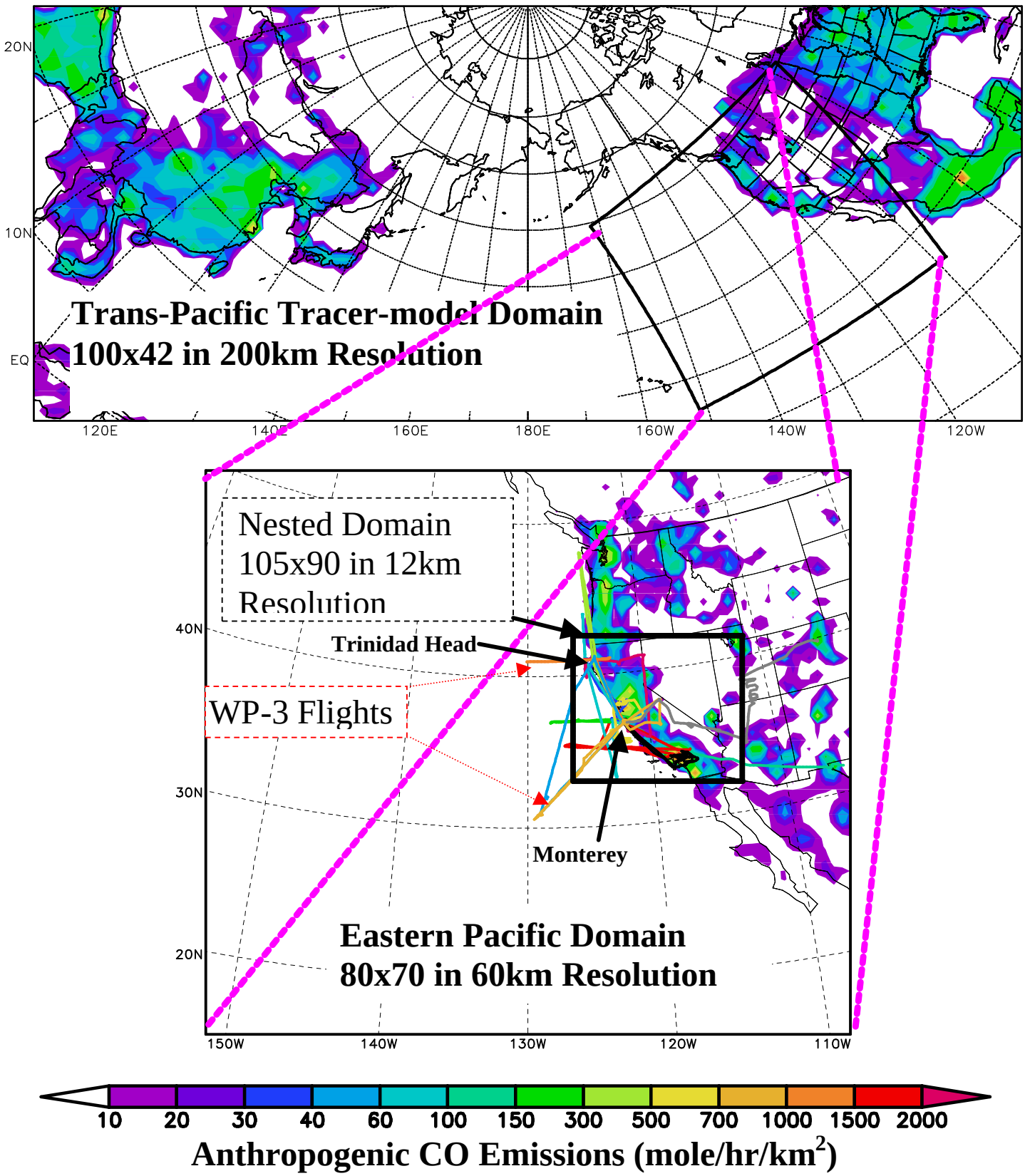
20N
10N
EQ
120E
140E
160E
180E
160W
140W
120W
Trans-Pacific Tracer-model Domain
100x42 in 200km Resolution
Nested Domain
105x90 in 12km
Resolution
Trinidad Head
WP-3 Flights
Monterey
40N
30N
20N
150W
140W
130W
120W
110W
Eastern Pacific Domain
80x70 in 60km Resolution
10
20
30
40
60
100
150
300
500
700
1000
1500
2000
Anthropogenic CO Emissions (mole/hr/km2)

Figure 1

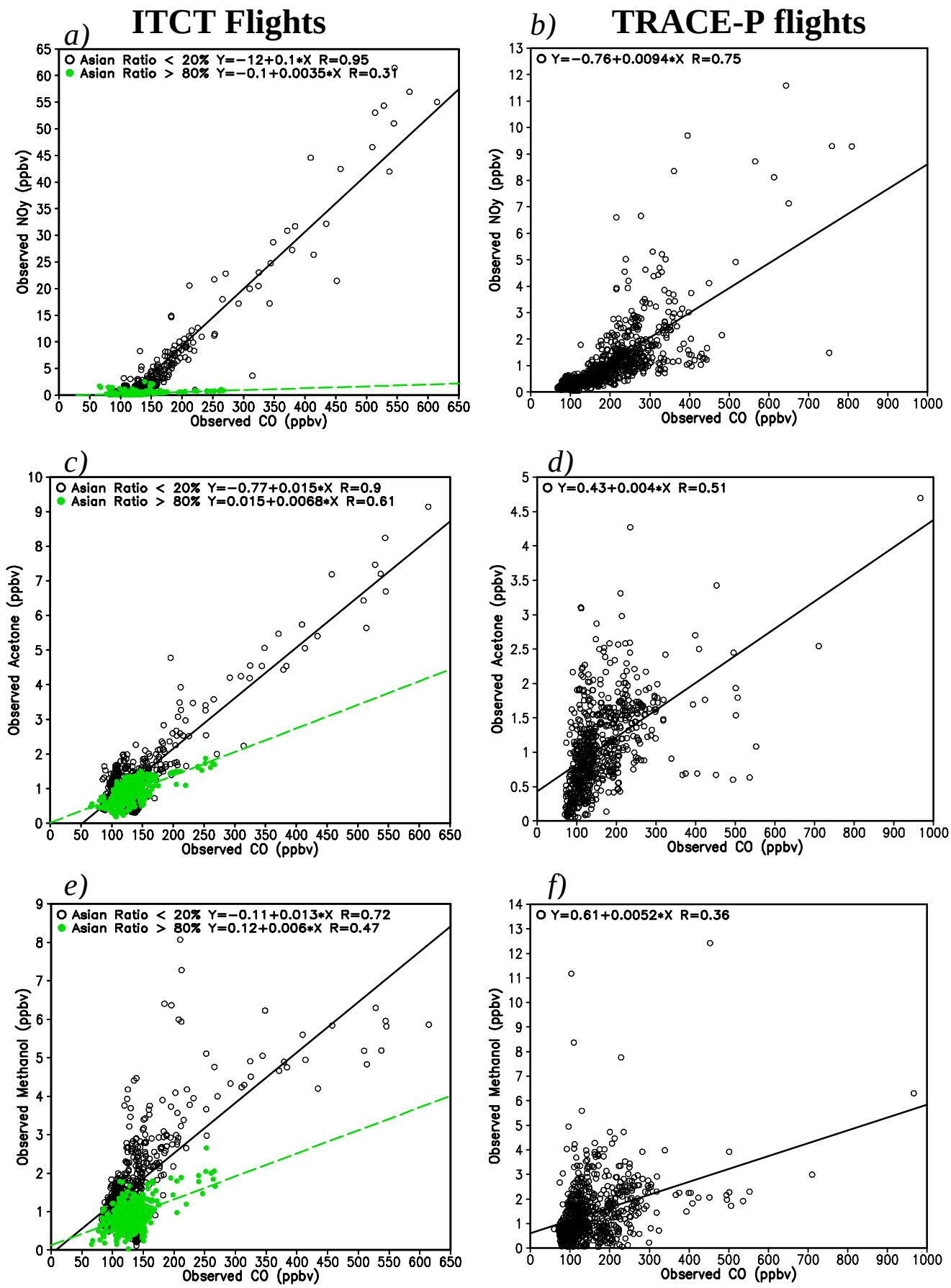

Figure 2 (continued in next page)

Figure 2 (continued)

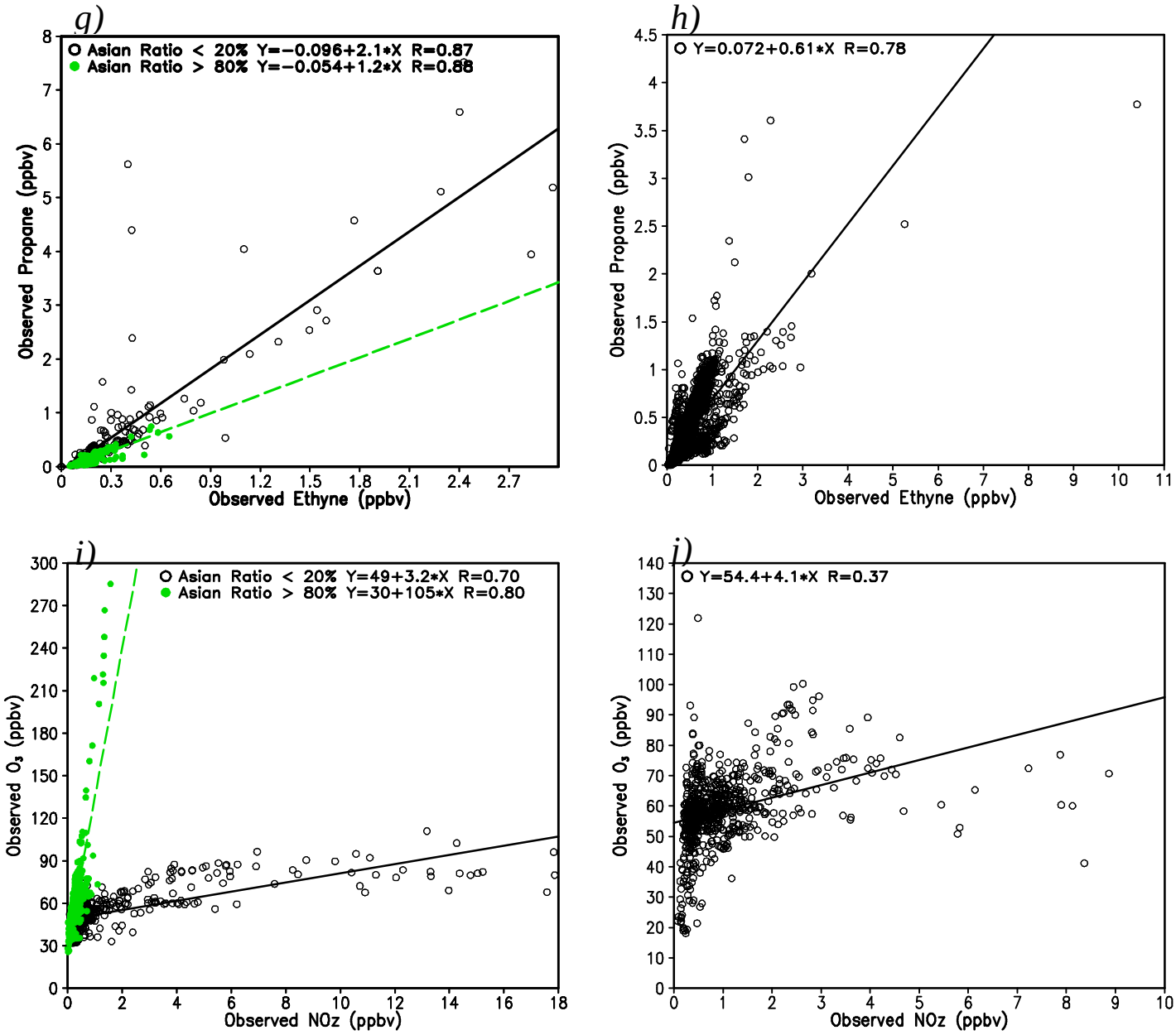

Figure 2

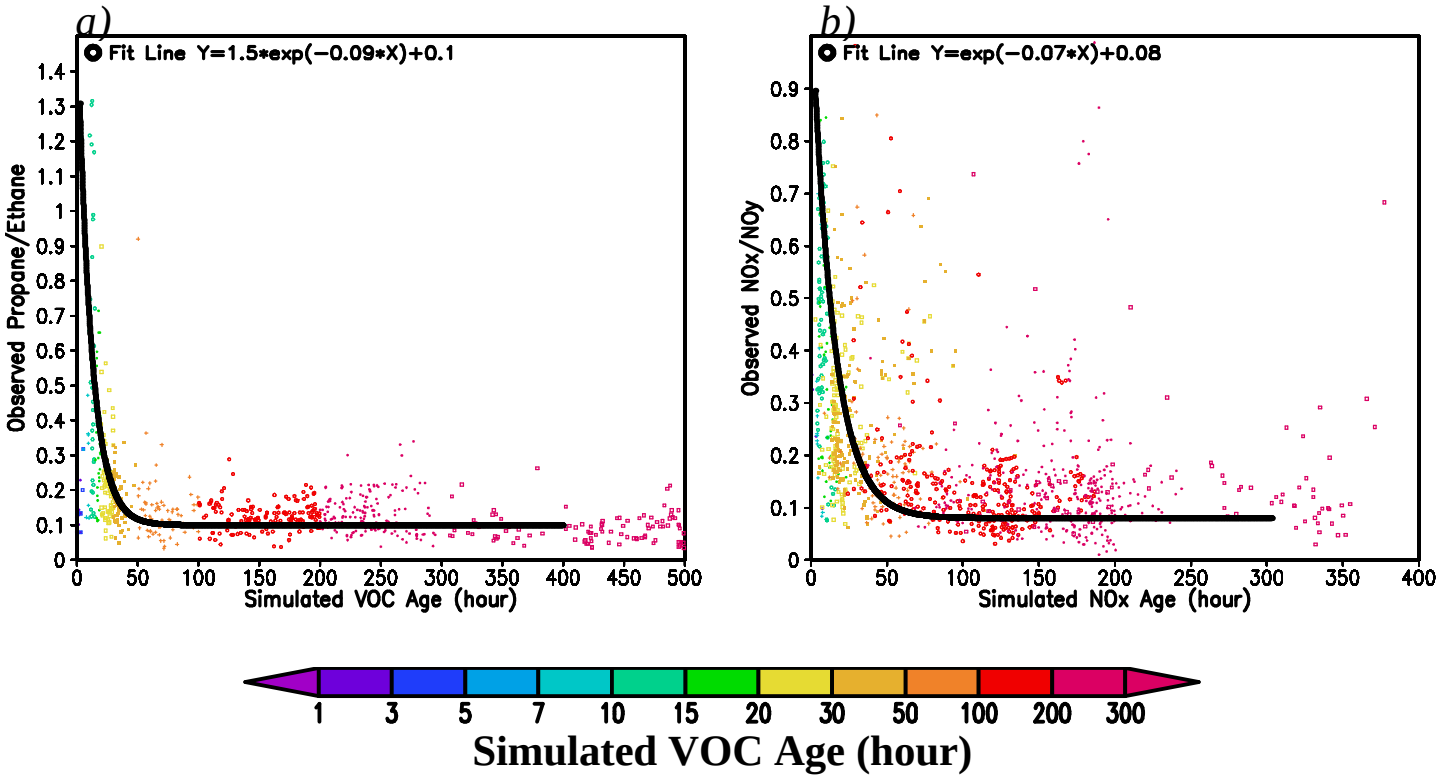
a)
Fit Line Y=1.5*exp(−0.09*X)+0.1
Observed Propane/Ethane
Simulated VOC Age (hour)
b)
Fit Line Y=exp(−0.07*X)+0.08
Observed NOx/NOy
Simulated NOx Age (hour)
1
3
5
7
10
15
20
30
50
100
200
300
Simulated VOC Age (hour)

Figure 3

a) **Simulated Anthropogenic CO and Its Asian Ratio in the 1 km layer**

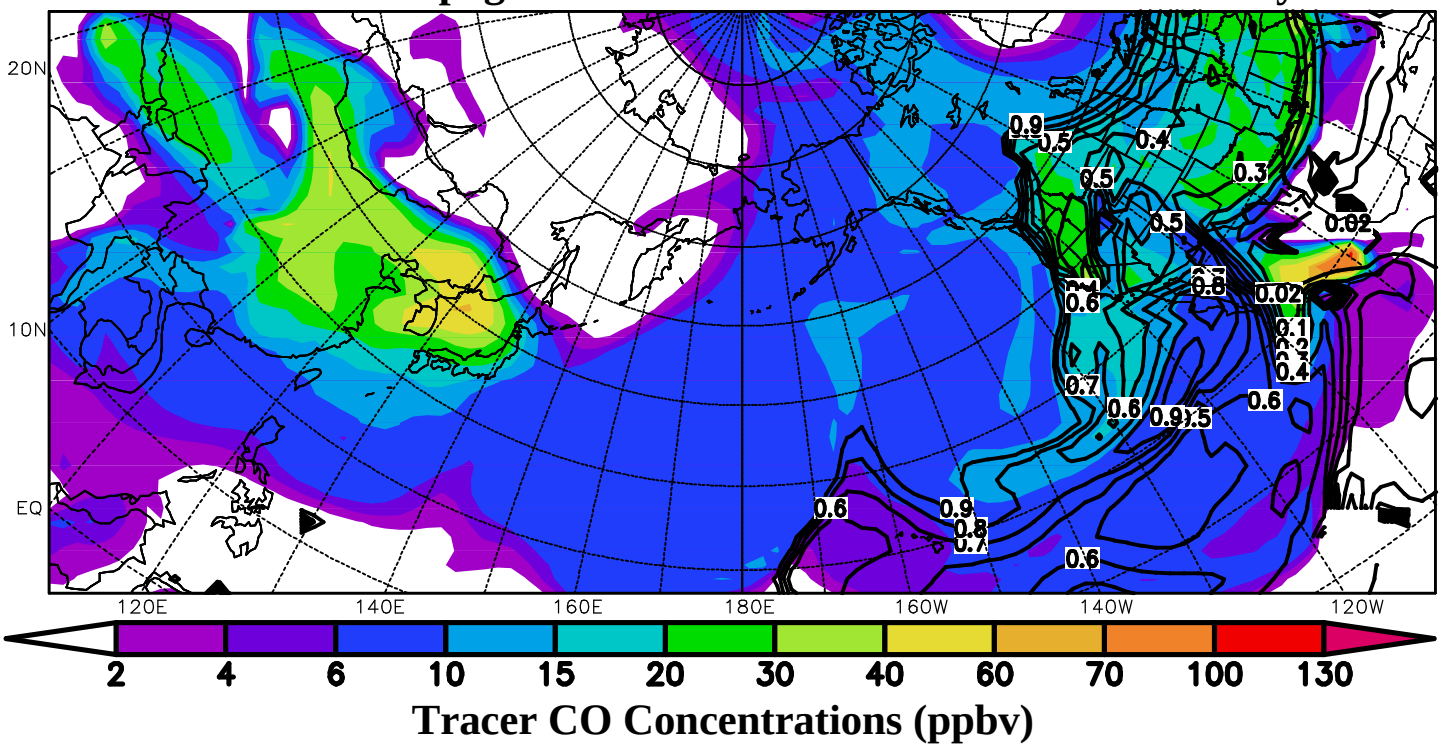

b) **Simulated Anthropogenic CO and Its Asian Ratio in the 5.4 km layer**

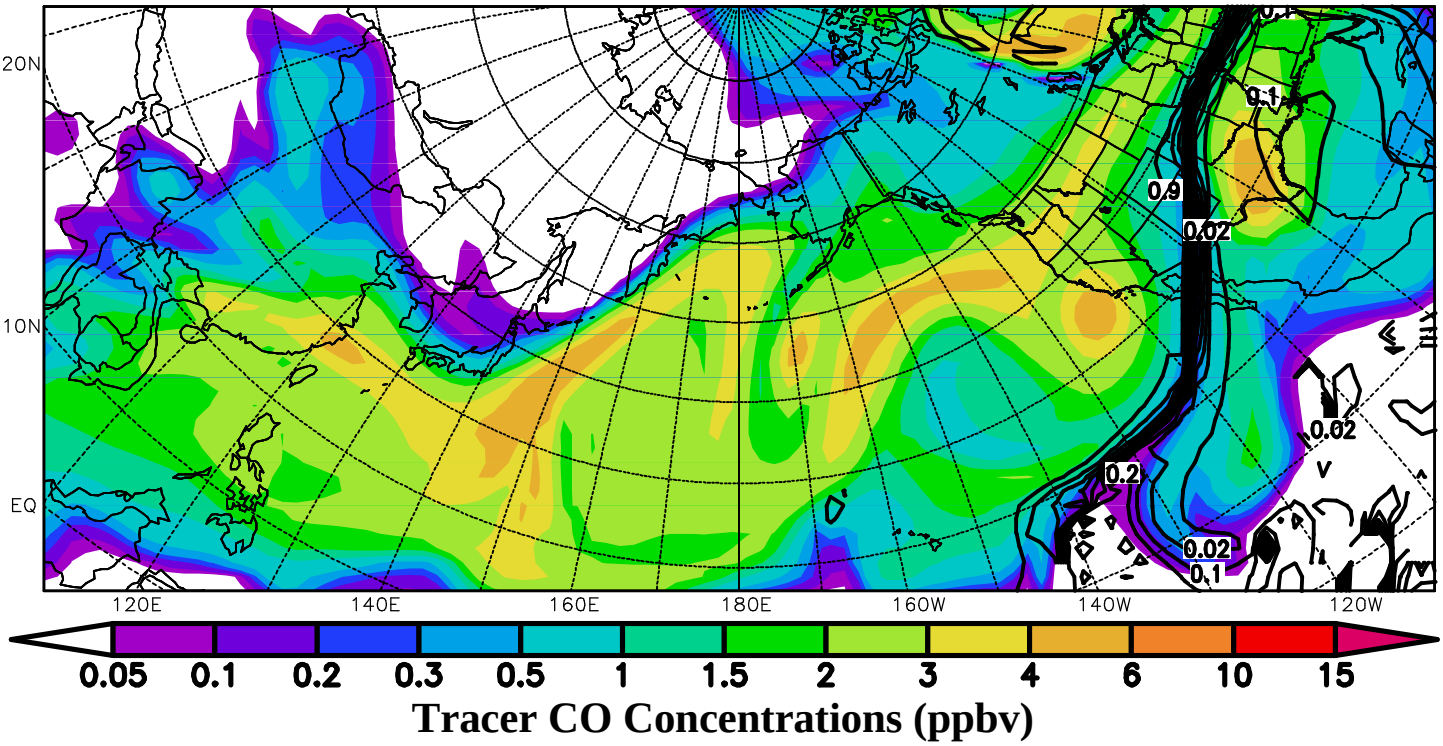

Figure 4

Figure 4 (continued)

c) **Simulated O_3 in the 1 km layer**

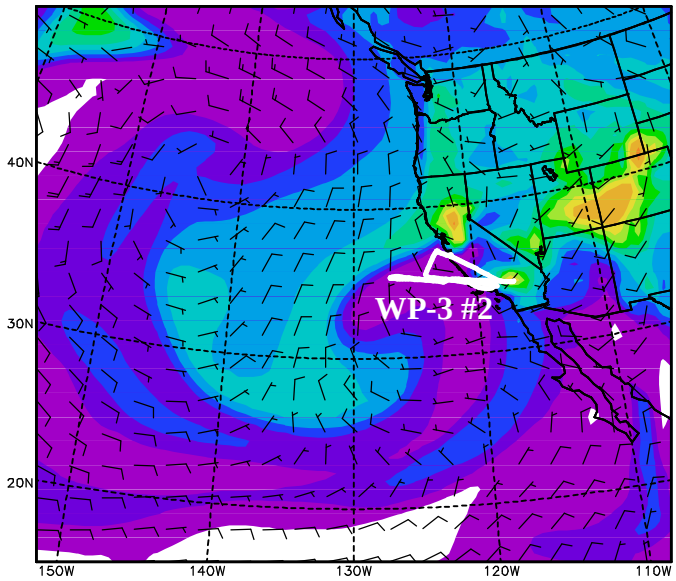

d) **Simulated O_3 in the 5.4 km layer**

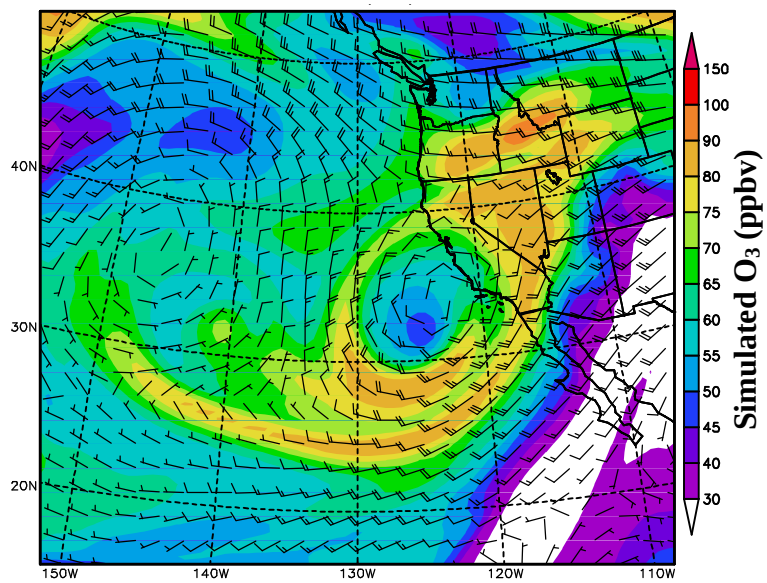

e)

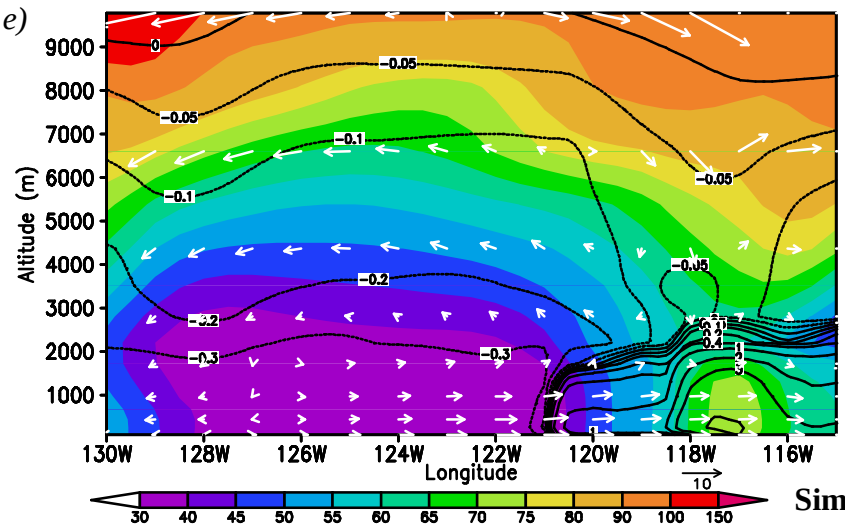

Simulated O_3 (color-coded) and its chemical net budget (contour) over latitude 35°N

Simulated O_3 (ppbv)

f)

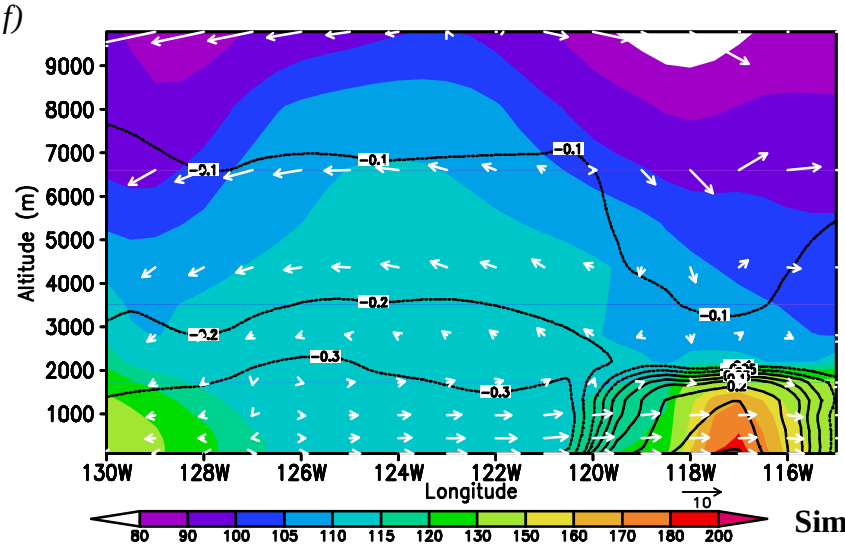

Simulated CO (color-coded) and its chemical net budget (contour) over latitude 35°N

Simulated CO (ppbv)

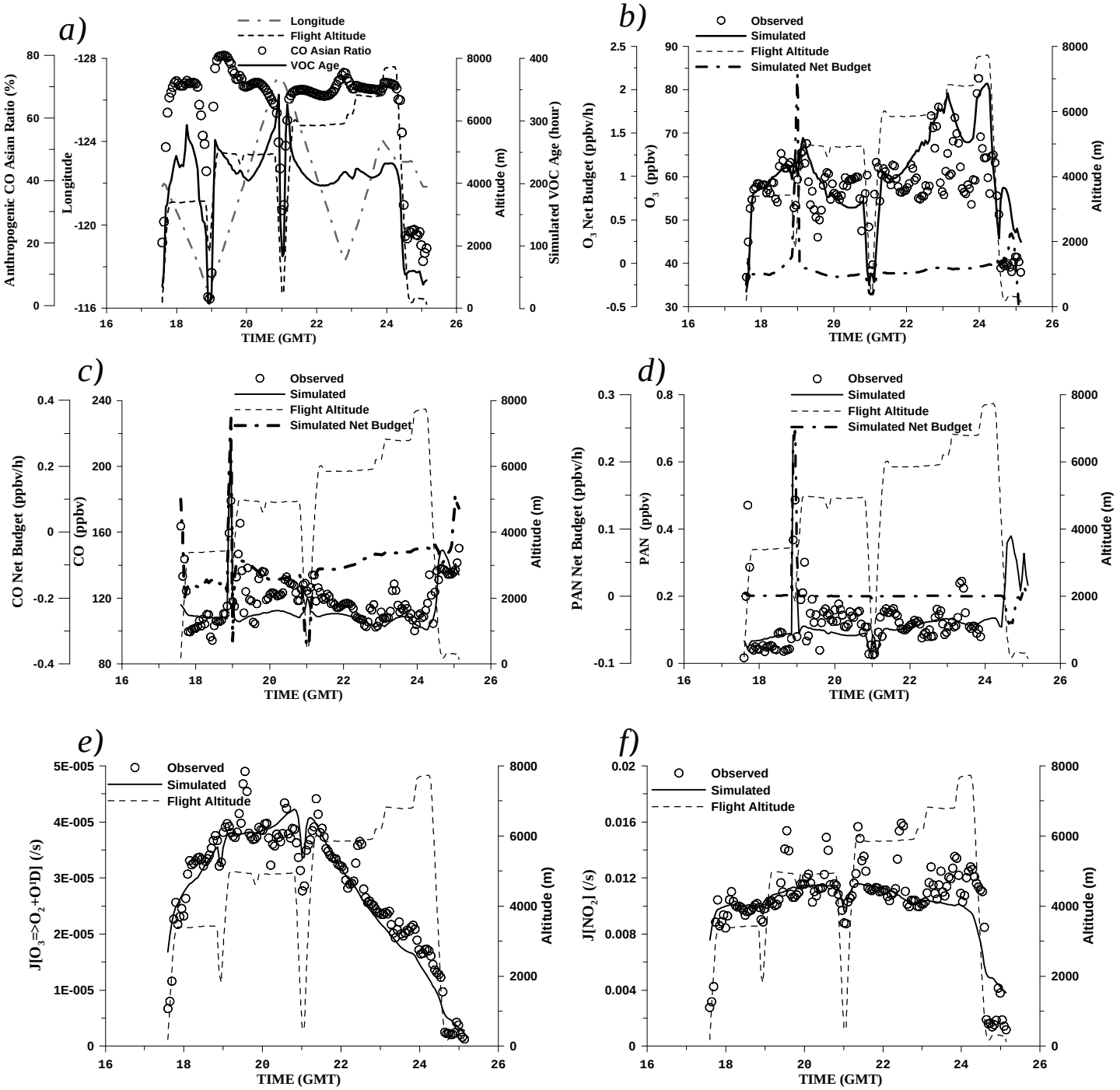
a)
Longitude
Flight Altitude
CO Asian Ratio
VOC Age
Anthropogenic CO Asian Ratio (%)
Longitude
Altitude (m)
Simulated VOC Age (hour)
TIME (GMT)
b)
Observed
Simulated
Flight Altitude
Simulated Net Budget
O3 Net Budget (ppbv/h)
O3 (ppbv)
Altitude (m)
TIME (GMT)
c)
Observed
Simulated
Flight Altitude
Simulated Net Budget
CO Net Budget (ppbv/h)
CO (ppbv)
Altitude (m)
TIME (GMT)
d)
Observed
Simulated
Flight Altitude
Simulated Net Budget
PAN Net Budget (ppbv/h)
PAN (ppbv)
Altitude (m)
TIME (GMT)
e)
Observed
Simulated
Flight Altitude
J[O3=>O2+O1D] (/s)
Altitude (m)
TIME (GMT)
f)
Observed
Simulated
Flight Altitude
J[NO2] (/s)
Altitude (m)
TIME (GMT)

Figure 5

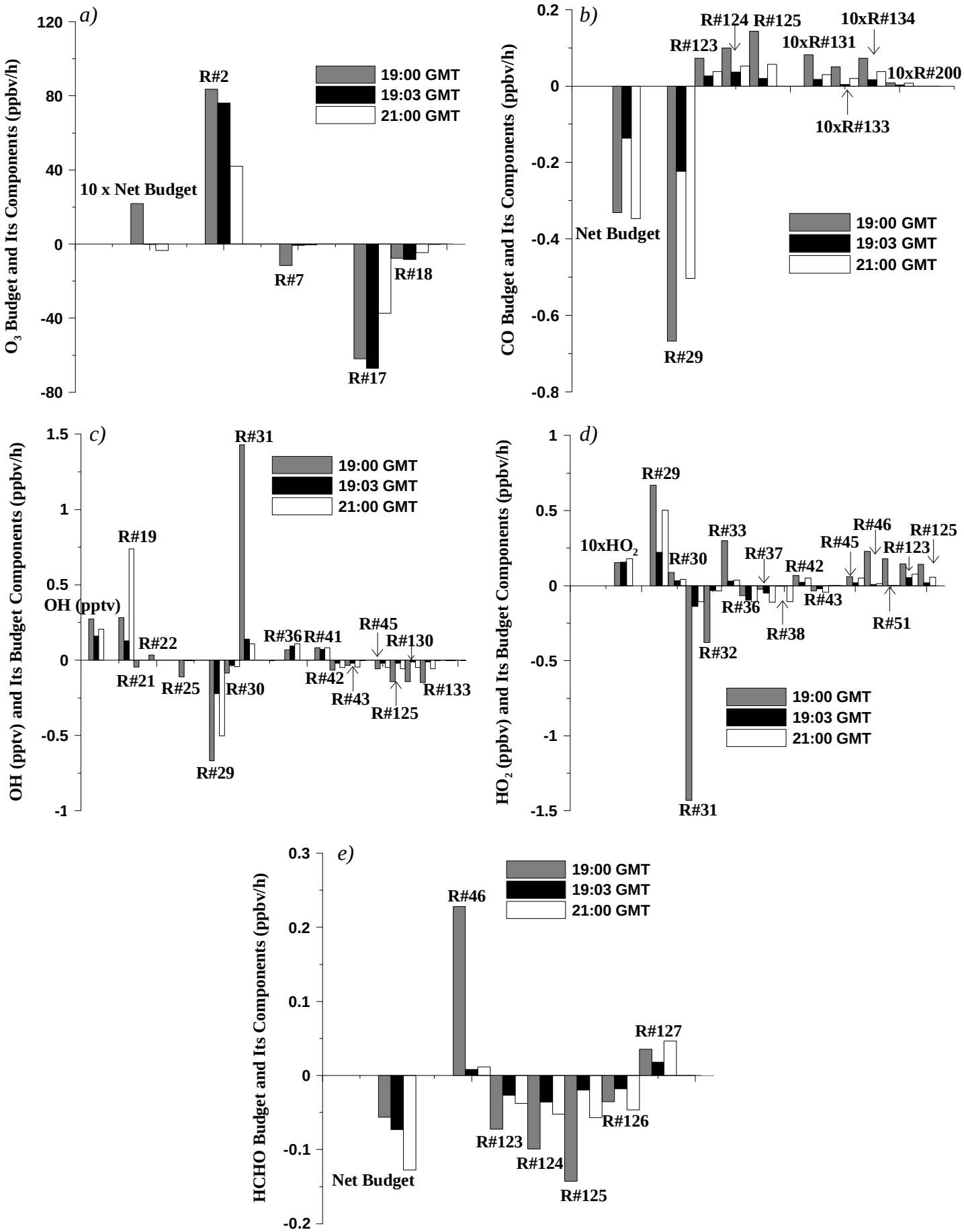
a)
O3 Budget and Its Components (ppbv/h)
120
80
40
0
-40
-80
10 x Net Budget
R#2
R#7
R#17
R#18
19:00 GMT
19:03 GMT
21:00 GMT
b)
CO Budget and Its Components (ppbv/h)
0.2
0
-0.2
-0.4
-0.6
-0.8
Net Budget
R#29
R#123
R#124
R#125
10xR#131
10xR#134
10xR#133
10xR#200
19:00 GMT
19:03 GMT
21:00 GMT
c)
OH (pptv) and Its Budget Components (ppbv/h)
1.5
1
0.5
0
-0.5
-1
OH (pptv)
R#19
R#21
R#22
R#25
R#29
R#30
R#31
R#36
R#41
R#42
R#43
R#45
R#125
R#130
R#133
19:00 GMT
19:03 GMT
21:00 GMT
d)
HO2 (ppbv) and Its Budget Components (ppbv/h)
1
0.5
0
-0.5
-1
-1.5
10xHO2
R#29
R#30
R#31
R#32
R#33
R#36
R#37
R#38
R#42
R#43
R#45
R#46
R#123
R#125
R#51
19:00 GMT
19:03 GMT
21:00 GMT
e)
HCHO Budget and Its Components (ppbv/h)
0.3
0.2
0.1
0
-0.1
-0.2
Net Budget
R#46
R#123
R#124
R#125
R#126
R#127
19:00 GMT
19:03 GMT
21:00 GMT

Figure 6

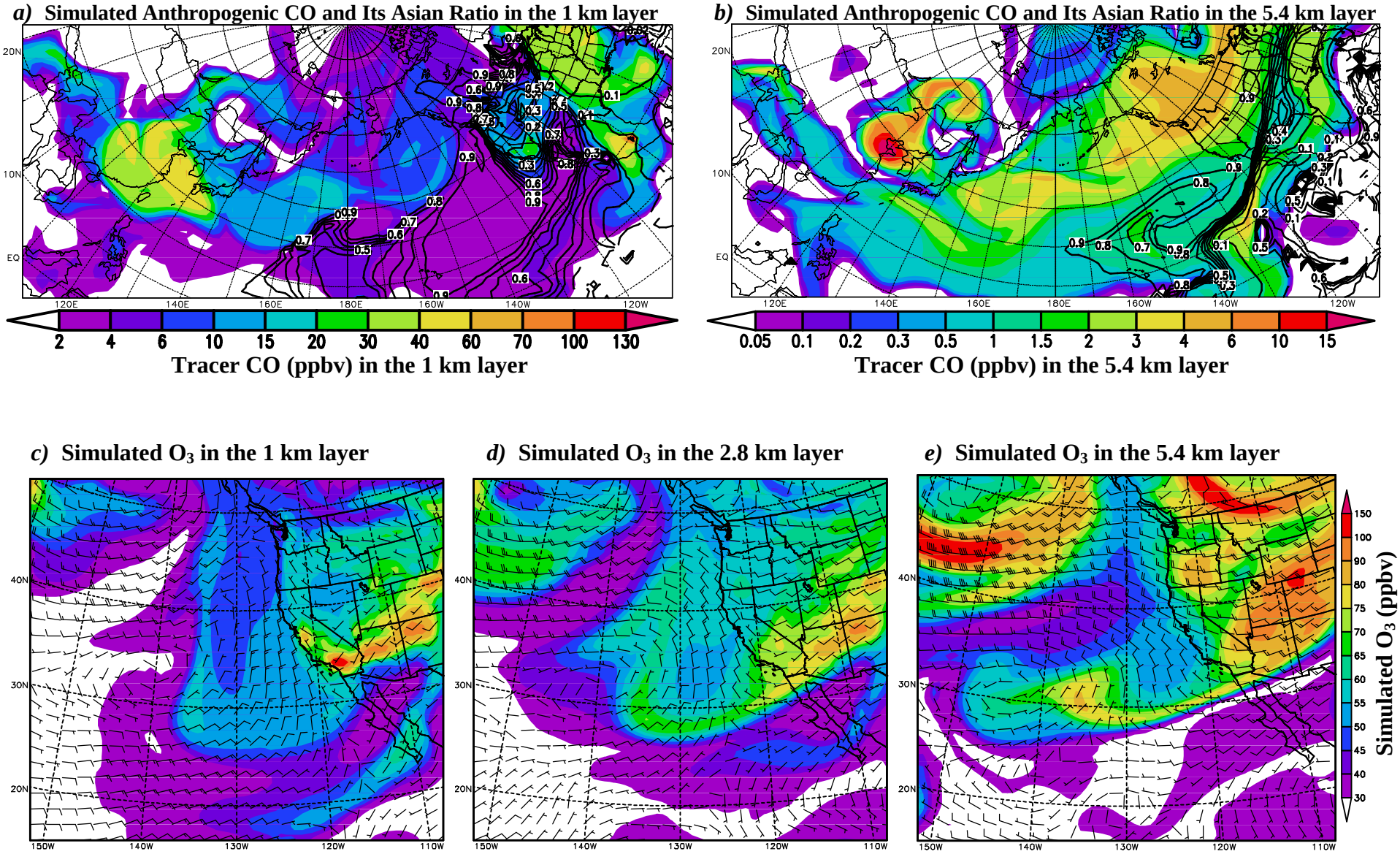
a) Simulated Anthropogenic CO and Its Asian Ratio in the 1 km layer
b) Simulated Anthropogenic CO and Its Asian Ratio in the 5.4 km layer
20N
10N
EQ
120E
140E
160E
180E
160W
140W
120W
2 4 6 10 15 20 30 40 60 70 100 130
Tracer CO (ppbv) in the 1 km layer
0.05 0.1 0.2 0.3 0.5 1 1.5 2 3 4 6 10 15
Tracer CO (ppbv) in the 5.4 km layer
c) Simulated O3 in the 1 km layer
d) Simulated O3 in the 2.8 km layer
e) Simulated O3 in the 5.4 km layer
40N
30N
20N
150W
140W
130W
120W
110W
150 100 90 80 75 70 65 60 55 50 45 40 30
Simulated O3 (ppbv)

Figure 7

Figure 7 (continued)

f) **Simulated O_3 Budget in the 1 km layer** *g)* **Simulated O_3 Budget in the 2.8 km layer** *h)* **Simulated O_3 Budget in the 5.4 km layer**

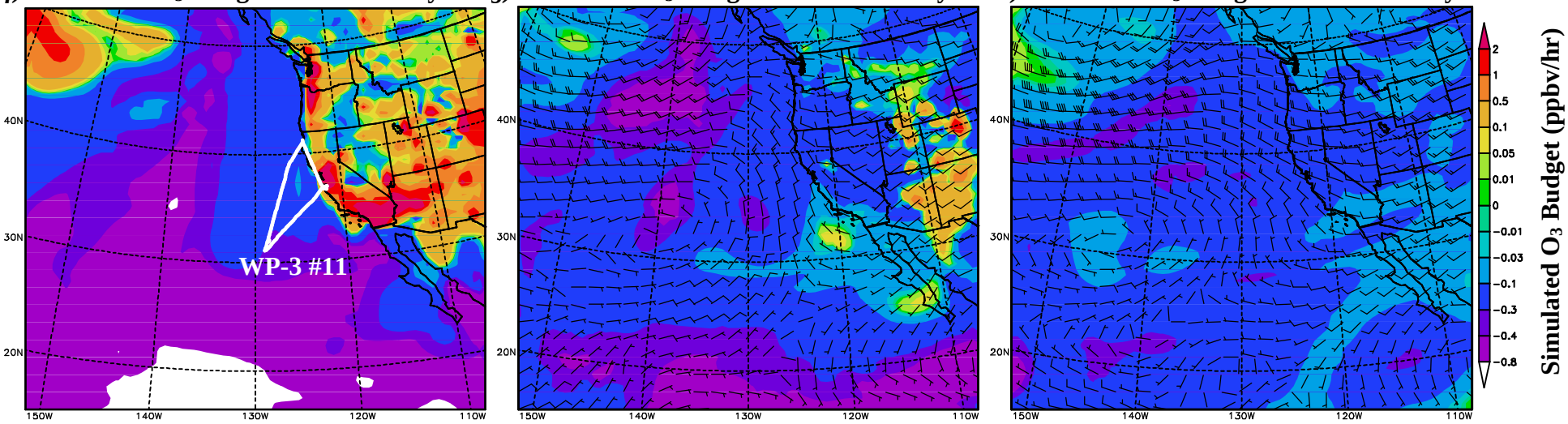

i) **Simulated CO Budget in the 1 km layer** *j)* **Simulated CO Budget in the 2.8 km layer** *k)* **Simulated CO Budget in the 5.4 km layer**

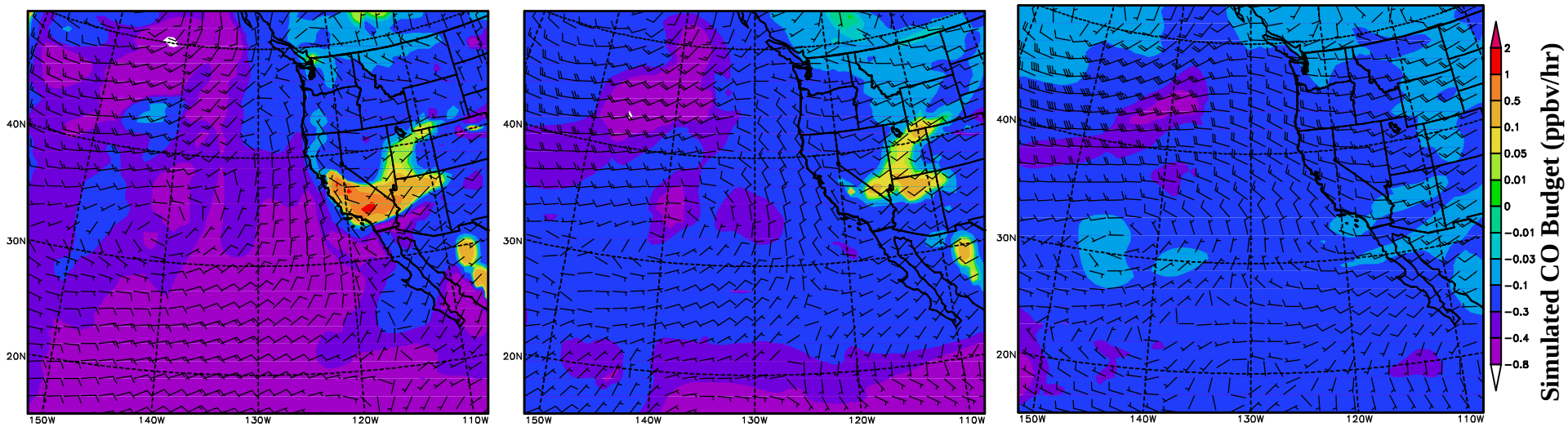

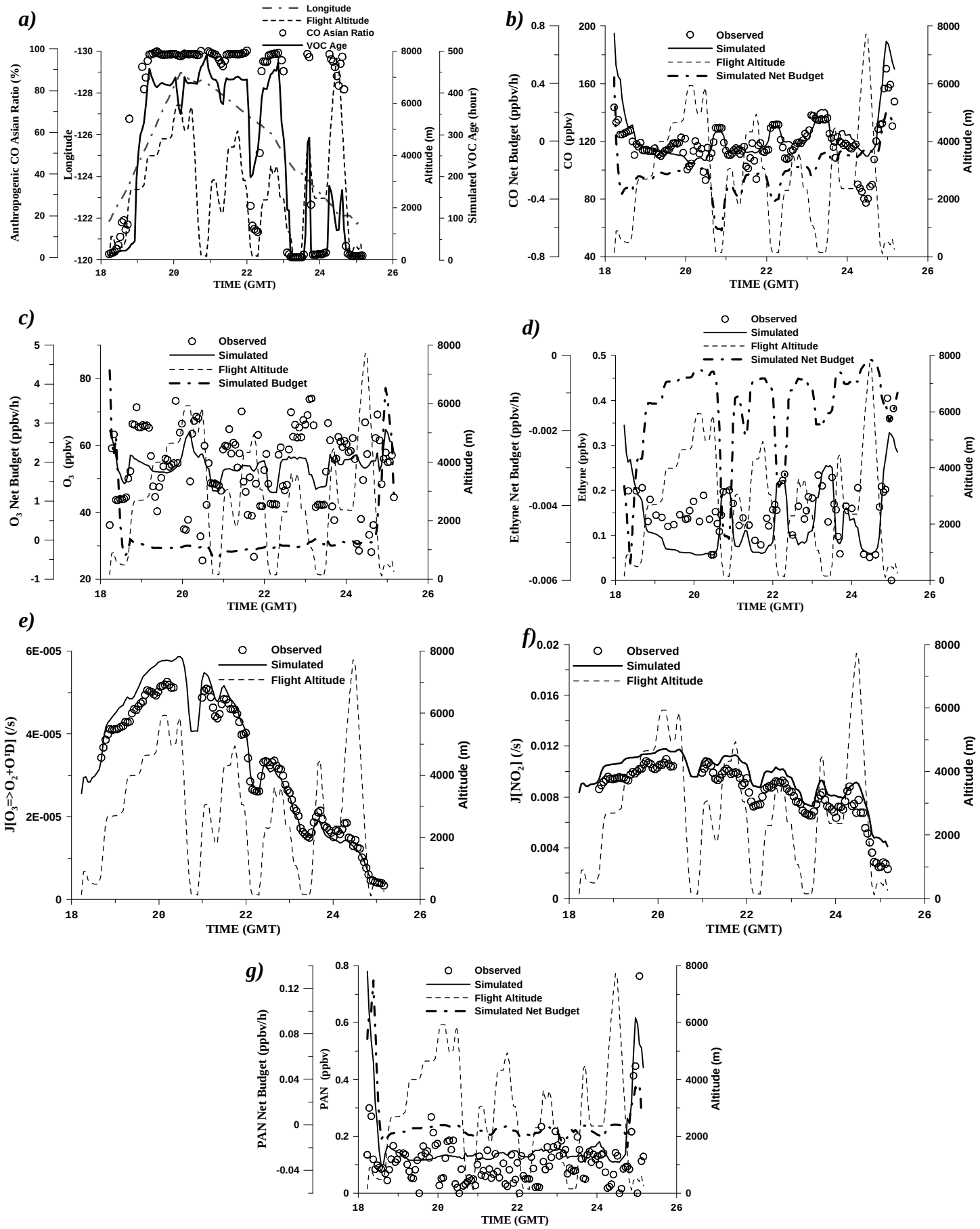
a)
Longitude
Flight Altitude
CO Asian Ratio
VOC Age
Anthropogenic CO Asian Ratio (%)
Longitude
Altitude (m)
Simulated VOC Age (hour)
TIME (GMT)
b)
Observed
Simulated
Flight Altitude
Simulated Net Budget
CO Net Budget (ppbv/h)
CO (ppbv)
Altitude (m)
TIME (GMT)
c)
Observed
Simulated
Flight Altitude
Simulated Budget
O3 Net Budget (ppbv/h)
O3 (ppbv)
Altitude (m)
TIME (GMT)
d)
Observed
Simulated
Flight Altitude
Simulated Net Budget
Ethyne Net Budget (ppbv/h)
Ethyne (ppbv)
Altitude (m)
TIME (GMT)
e)
Observed
Simulated
Flight Altitude
J[O3=>O2+O1D] (/s)
Altitude (m)
TIME (GMT)
f)
Observed
Simulated
Flight Altitude
J[NO2] (/s)
Altitude (m)
TIME (GMT)
g)
Observed
Simulated
Flight Altitude
Simulated Net Budget
PAN Net Budget (ppbv/h)
PAN (ppbv)
Altitude (m)
TIME (GMT)

Figure 8

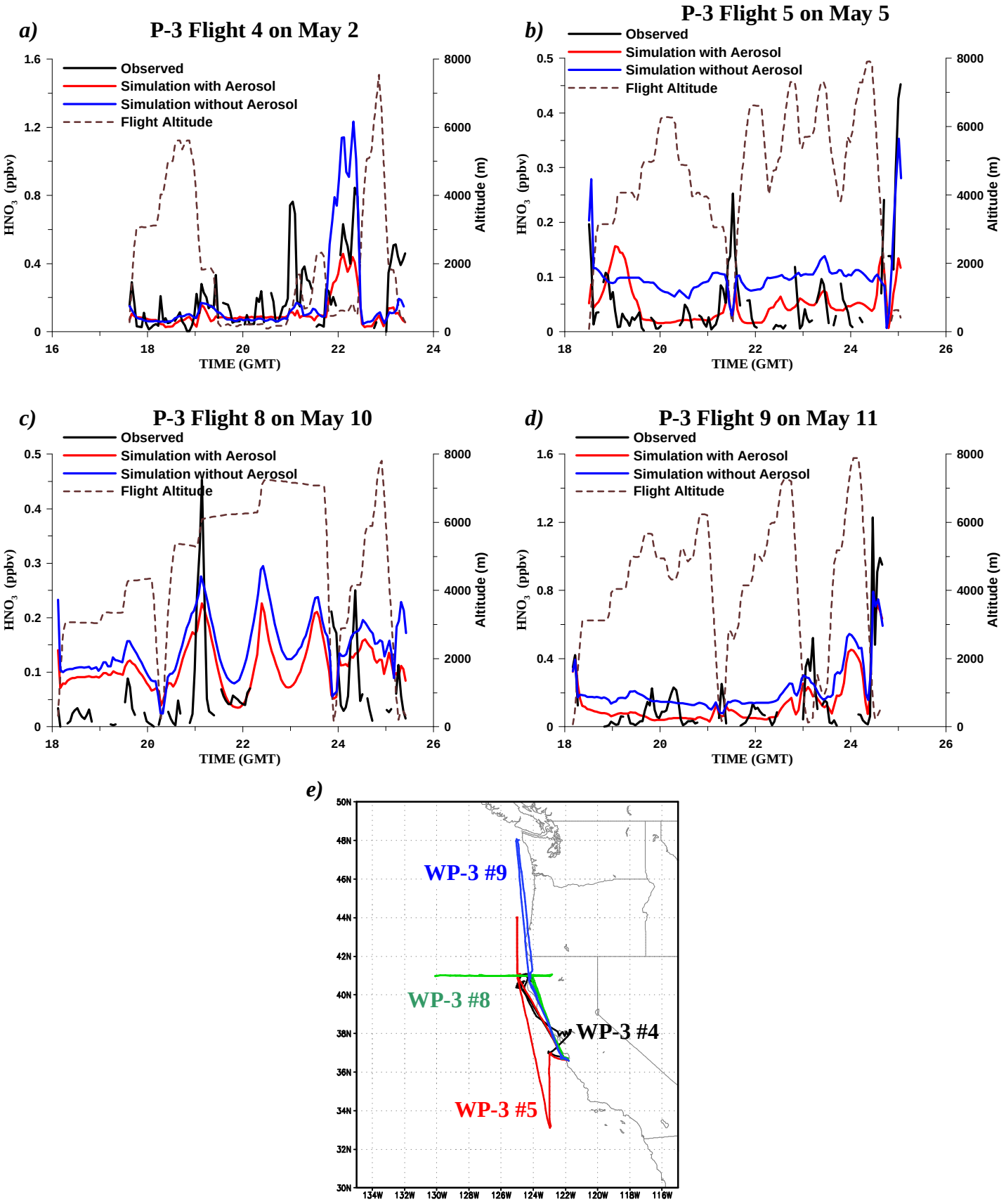
a)
P-3 Flight 4 on May 2
b)
P-3 Flight 5 on May 5
c)
P-3 Flight 8 on May 10
d)
P-3 Flight 9 on May 11
Observed
Simulation with Aerosol
Simulation without Aerosol
Flight Altitude
HNO3 (ppbv)
Altitude (m)
TIME (GMT)
e)
WP-3 #9
WP-3 #8
WP-3 #4
WP-3 #5

Figure 9

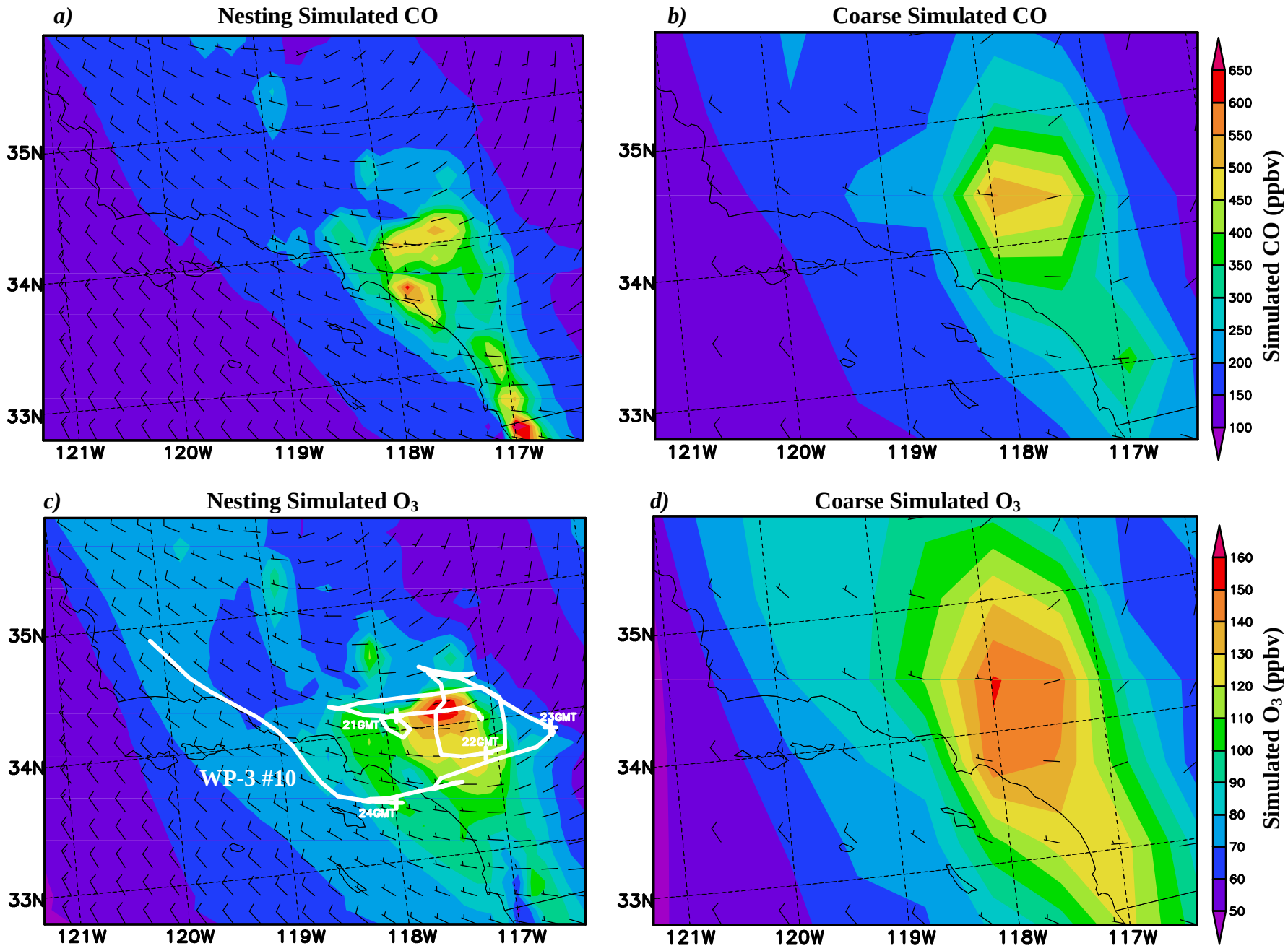
a)
Nesting Simulated CO
b)
Coarse Simulated CO
c)
Nesting Simulated O3
d)
Coarse Simulated O3
35N
34N
33N
121W
120W
119W
118W
117W
Simulated CO (ppbv)
650
600
550
500
450
400
350
300
250
200
150
100
Simulated O3 (ppbv)
160
150
140
130
120
110
100
90
80
70
60
50
WP-3 #10
21GMT
22GMT
23GMT
24GMT

Figure 10

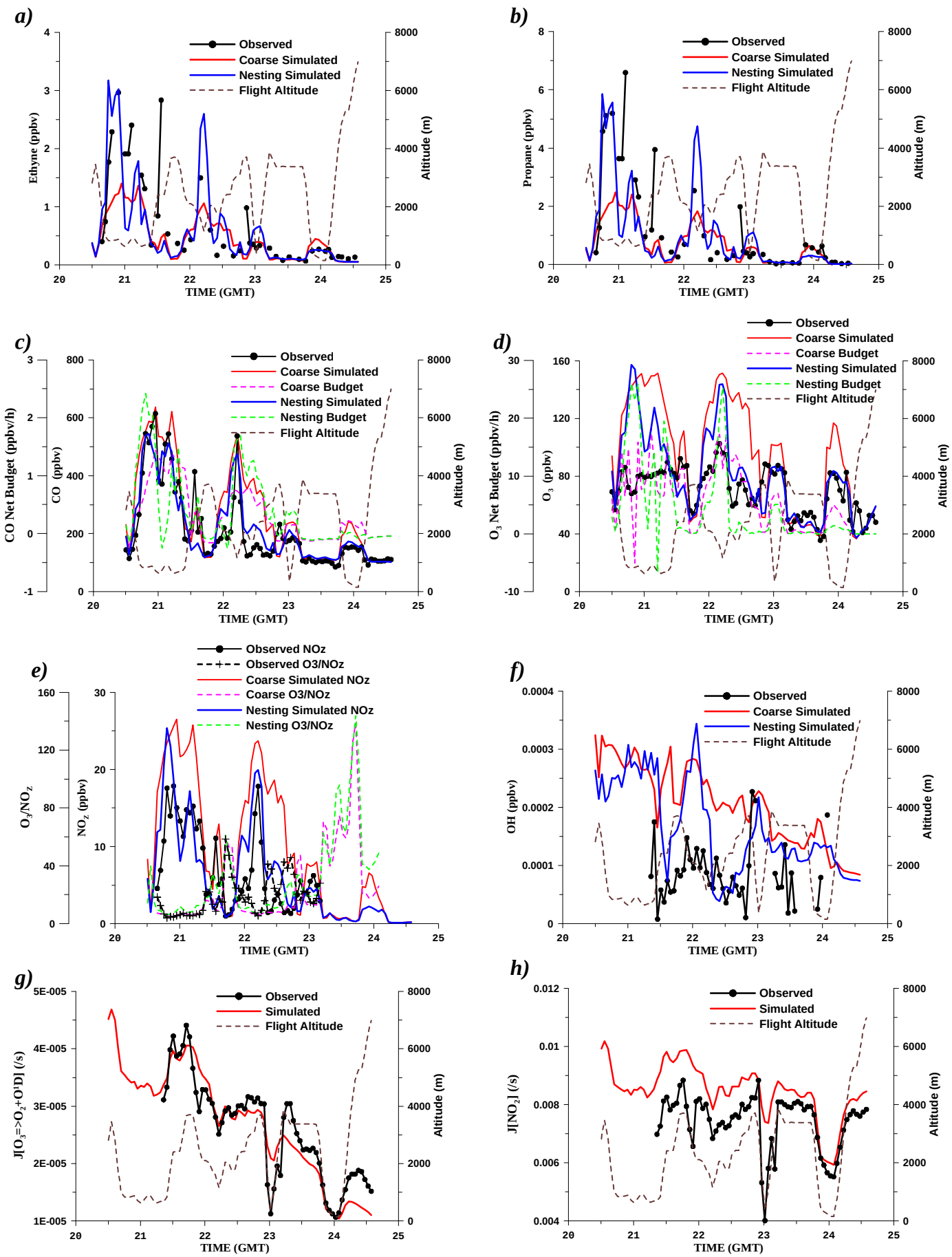
a)
Observed
Coarse Simulated
Nesting Simulated
Flight Altitude
Ethyne (ppbv)
Altitude (m)
TIME (GMT)
b)
Propane (ppbv)
c)
Coarse Budget
Nesting Budget
CO Net Budget (ppbv/h)
CO (ppbv)
d)
O_3 Net Budget (ppbv/h)
O_3 (ppbv)
e)
Observed NOz
Observed O3/NOz
Coarse Simulated NOz
Coarse O3/NOz
Nesting Simulated NOz
Nesting O3/NOz
O_3/NO_Z
NO_Z (ppbv)
f)
OH (ppbv)
g)
Simulated
$J[O_3 => O_2 + O^1D]$ (/s)
h)
$J[NO_2]$ (/s)

Figure 11

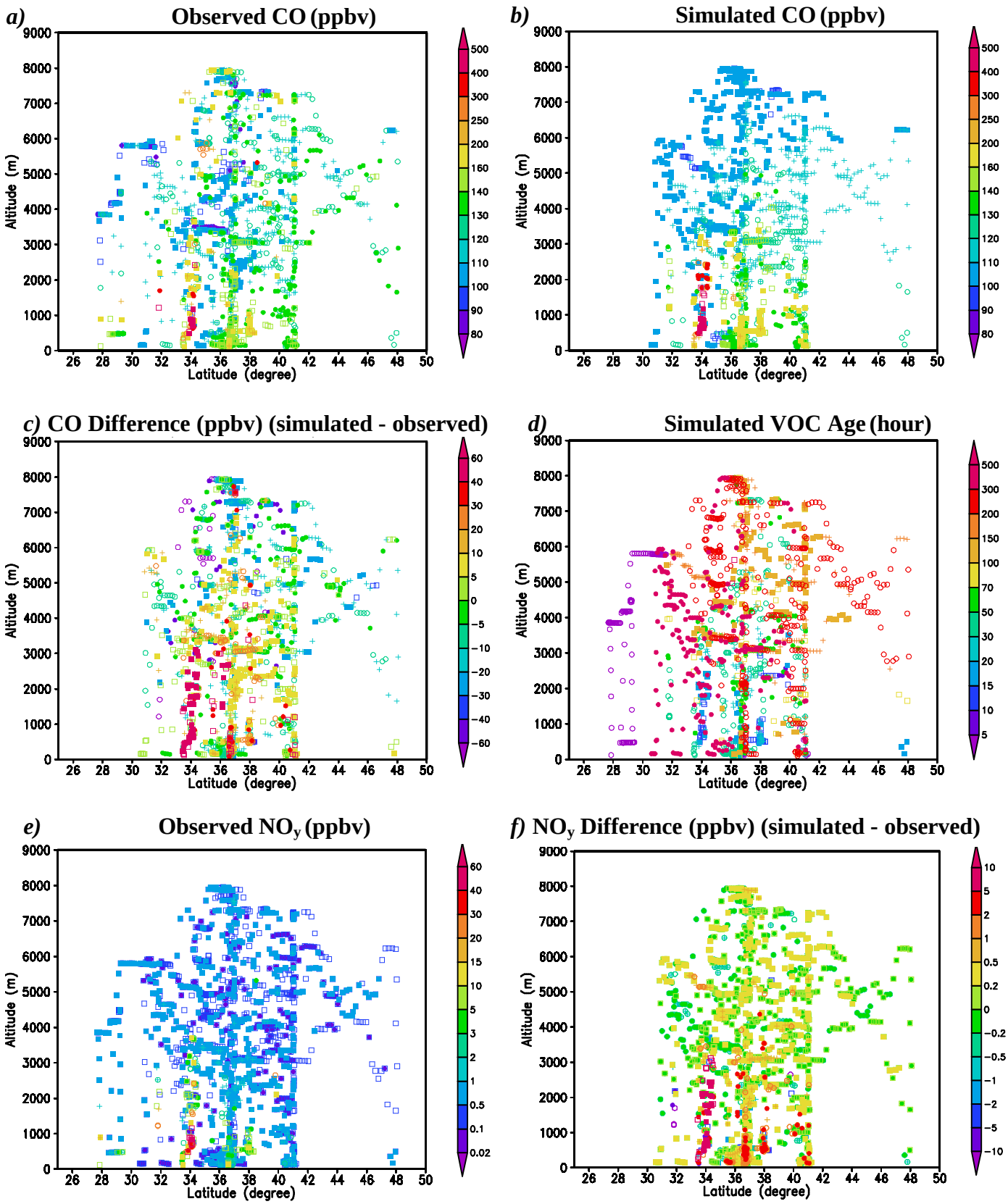
a) Observed CO (ppbv)
b) Simulated CO (ppbv)
c) CO Difference (ppbv) (simulated - observed)
d) Simulated VOC Age (hour)
e) Observed NOy (ppbv)
f) NOy Difference (ppbv) (simulated - observed)
Altitude (m)
Latitude (degree)

Figure 12

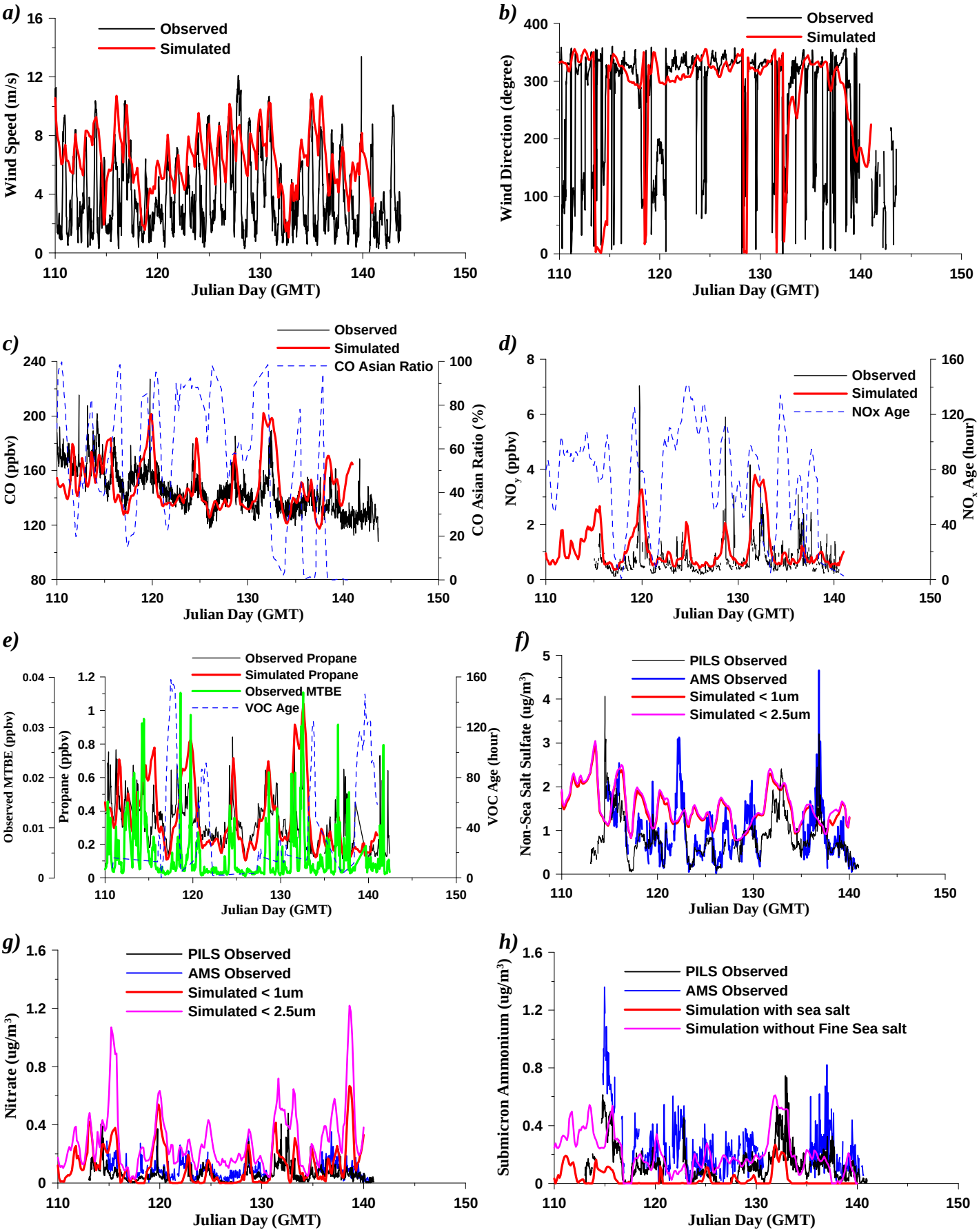
a)
Observed
Simulated
Wind Speed (m/s)
Julian Day (GMT)
b)
Observed
Simulated
Wind Direction (degree)
Julian Day (GMT)
c)
Observed
Simulated
CO Asian Ratio
CO (ppbv)
CO Asian Ratio (%)
Julian Day (GMT)
d)
Observed
Simulated
NOx Age
NO$_y$ (ppbv)
NO$_x$ Age (hour)
Julian Day (GMT)
e)
Observed Propane
Simulated Propane
Observed MTBE
VOC Age
Observed MTBE (ppbv)
Propane (ppbv)
VOC Age (hour)
Julian Day (GMT)
f)
PILS Observed
AMS Observed
Simulated < 1um
Simulated < 2.5um
Non-Sea Salt Sulfate (ug/m^3)
Julian Day (GMT)
g)
PILS Observed
AMS Observed
Simulated < 1um
Simulated < 2.5um
Nitrate (ug/m^3)
Julian Day (GMT)
h)
PILS Observed
AMS Observed
Simulation with sea salt
Simulation without Fine Sea salt
Submicron Ammonium (ug/m^3)
Julian Day (GMT)

Figure 13